Geoscience Frontiers 14 (2023) 101596

HOSTED BY

Contents lists available at ScienceDirect

Geoscience Frontiers

journal homepage: www.elsevier.com/locate/gsf

Research Paper

Linking the Gawler Craton and Mount Isa Province through hydrothermal systems in the Peake and Denison Domain, northeastern Gawler Craton

Mitchell J. Bockmann [a,b,*], Justin L. Payne [c,d], Martin Hand [a,b], Laura J. Morrissey [a,d], Antonio P. Belperio [e]

[a] Department of Earth Sciences, University of Adelaide, Adelaide, SA, Australia
[b] Mineral Exploration Cooperative Research Centre, University of Adelaide, Adelaide, SA, Australia
[c] UniSA STEM, University of South Australia, Adelaide, SA, Australia
[d] Mineral Exploration Cooperative Research Centre, Future Industries Institute, University of South Australia, Adelaide, SA, Australia
[e] Demetallica Ltd, Norwood, SA, Australia

ARTICLE INFO

Article history:
Received 29 July 2022
Revised 31 January 2023
Accepted 28 March 2023
Available online 30 March 2023
Handling Editor: Vinod Samuel

Keywords:
Peake and Denison
Gawler Craton
Mount Isa
IOCG
Tectonic reconstruction
Titanite

ABSTRACT

Tectonic reconstructions of Proterozoic Australia commonly place the Peake and Denison Domain of the northeastern Gawler Craton at the interface between the North and South Australian cratons prior to the reconfiguration of Australia's main tectonic components in the Mesoproterozoic. However, this reconstruction is largely based on palaeomagnetic data as the geological correlations between these regions are currently limited, particularly during the Mesoproterozoic. The early Mesoproterozoic period is significant as it corresponds to major IOCG mineralization in the eastern Gawler Craton between 1600 Ma and 1575 Ma, and IOCG mineralization in the Mount Isa Province largely between 1550 Ma and 1490 Ma. Therefore, determining the relationship of the Peake and Denison Domain to the Gawler Craton and Mount Isa Province during this period is essential to evaluating mineral prospectivity in the northeastern Gawler Craton. New U–Pb LA-ICP-MS geochronology on zircon and titanite improves our understanding of the tectonothermal and hydrothermal history the Peake and Denison Domain during the late-Palaeoproterozoic, early-Mesoproterozoic and the Cambrian–Ordovician periods. Titanite formed within largely calc-silicate alteration assemblages indicates the Peake and Denison Domain has a protracted history of hydrothermal activity, recording events at c. 1565 Ma, 1530–1515 Ma, c. 1500 Ma, c. 1465 Ma and c. 490 Ma. The highly calcic nature of the c. 1565–1500 Ma alteration in the Peake and Denison Domain shares strong similarities in age and character to the regional calcic-sodic alteration recorded in the Mount Isa Province. We suggest the two regions were influenced by similar hydrothermal systems during the early Mesoproterozoic, supporting reconstruction models that place the Peake and Denison Domain near the Mount Isa Province during the early-Mesoproterozoic. This highlights the prospectivity of the Peake and Denison Domain for Isan-style IOCG mineralization, but requires consideration of the post-1500 Ma rotation of prospective structures.

1. Introduction

Tectonic reconstruction models are often argued to be valuable for the purposes of mineral exploration targeting at the terrane scale, as metallogenic belts can be fragmented and dispersed by plate tectonics (Groves and Bierlein, 2007; Cawood and Hawkesworth, 2015). Nevertheless, continental reconstructions themselves rarely draw upon hydrothermal or mineralization events as piercing points to link crustal blocks. However, these hydrothermal or mineralization events are generally the culmination of a broader mineral system (e.g. Wyborn et al., 1994), which is largely a combination of geological processes that are primarily driven by plate tectonics. Consequently, hydrothermal and mineralization events can be inherently indicative of their tectonic environment, and therefore can be used in combination with other forms of tectonic evidence (i.e. magmatism, metamorphism and sedimentary basin formation) to reconstruct ancient tectonic settings. For the purposes of mineral exploration, similarities in the

* Corresponding author at: Department of Earth Sciences, University of Adelaide, Adelaide, SA, Australia.
E-mail address: mitchell.bockmann@adelaide.edu.au (M.J. Bockmann).

https://doi.org/10.1016/j.gsf.2023.101596

timing of magmatic and tectonic events are obviously promising, but do not necessarily guarantee the same crustal or mantle conditions that lead to the formation of mineral deposits. However, correlation in age and alteration styles between regions affected by hydrothermal events and those with well recognized mineralization can assist mineral prospectivity evaluation in the correlative regions that seemingly lack significant mineralization.

A contentious subject in Proterozoic Australia reconstructions is the relationship between the North Australian Craton (NAC) and South Australian Craton (SAC) during the Mesoproterozoic. These crustal blocks are considered to have been connected with East Antarctica to form the Diamantina Craton (Cawood and Korsch, 2008). The oldest geological correlations suggest the crustal elements of the Diamantina Craton were contiguous as early as *c.* 2.52 Ga (Cawood and Korsch, 2008; Payne et al., 2009; Hollis et al., 2010; Reid et al., 2014), with numerous correlations that suggest it remained contiguous throughout the Palaeoproterozoic (Giles et al., 2004; Betts and Giles, 2006; Cawood and Korsch, 2008; Payne et al., 2009; Betts et al., 2015; Armit et al., 2017). Palaeomagnetic data suggest the SAC and East Antarctica (collectively termed the Mawson Continent; Payne et al., 2009) was rotated from a position adjacent to the NAC to its present configuration sometime after *c.* 1.59 Ga (Wingate and Evans, 2003; Giles et al., 2004; Payne et al., 2009). It is broadly assumed this disaggregation occurred during the break-up of the Nuna (Columbia) supercontinent, which is recorded by the development of rift basins and magmatism within the NAC and SAC between *c.* 1.49 Ga and 1.45 Ga (Jackson et al., 1999; Beyer et al., 2018; Morrissey et al., 2019). It is reasonable to assume this supercontinent-scale extensional event likely represents the minimum age for the Diamantina Craton. However prior to this break-up, extensive Iron oxide-Copper-Gold-Uranium-Rare Earth Element (IOCG-UREE) mineralization occurred across these two crustal blocks. In the SAC, mineralization occurred at *c.* 1.63–1.58 Ga (Fig. 1; Skirrow et al., 2000; Reid, 2019), whereas the main period of mineralization in the Mount Isa Province of the NAC occurred between *c.* 1.55 Ga and 1.49 Ga (Perkins et al., 1999; Mark et al., 2006; Duncan et al., 2011). Therefore, establishing the relationship between the NAC and SAC during this period is fundamental for understanding the tectonic controls on mineralization and determining the mineral prospectivity in the regions connecting the NAC and SAC at this time.

The Peake and Denison Domain in the northeastern Gawler Craton (Fig. 1) is located in a key position for understanding the relationship between the NAC and SAC during the early Mesoproterozoic, as most reconstruction models show general consensus on the approximate position of the Peake and Dension Domain between the NAC and SAC during the late Palaeoproterozoic (Giles et al., 2004; Payne et al., 2009; Betts et al., 2015). However, the Mesoproterozoic evolution of the Peake and Denison Domain is poorly understood and therefore its relationship with the NAC and SAC during this period is not well established. We present ages for magmatism, deformation and hydrothermal alteration from the Peake and Denison Domain that improve our understanding of the relationship between the NAC and SAC during the early Mesoproterozoic. These new data strengthen previously established correlations between the Peake and Denison Domain and Mount Isa Province and extend the duration of this connection to *c.* 1500 Ma. These results have implications for the tectonic reconstruction of Australia and the mineral potential in the northeastern Gawler Craton.

2. Geological background

2.1. Correlations between the NAC and SAC

The concealment of the northern Gawler Craton and southern Mount Isa Province beneath thick sedimentary cover makes it difficult to understand the direct relationships between the NAC and SAC. Consequently their interactions are largely interpreted through broad correlations of geological phenomena recorded across the two crustal blocks.

The Gawler Craton between *c.* 2.00 Ga and 1.73 Ga was in a dominantly extensional tectonic regime, resulting in *c.* 1.85 Ga back-arc magmatism (Reid et al., 2008) and the widespread development of sedimentary basins that host a number of volcano-

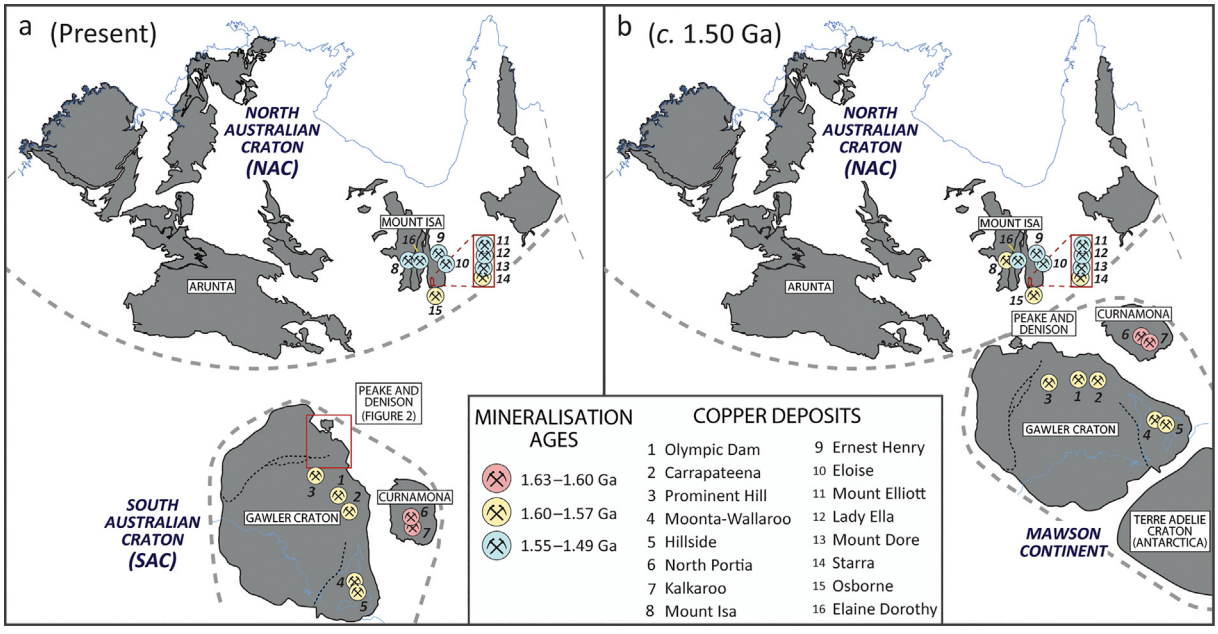

Fig. 1. Distribution of latest-Palaeoproterozoic to early-Mesoproterozoic copper deposits within the North Australian Craton (NAC) and South Australian Craton (SAC). (a) Present-day configuration. (b) Reconstructed configuration of the NAC and SAC at *c.* 1.50 Ga. In this reconstruction the Peake and Denison Domain is situated near the interface of the NAC and SAC and between three mineralized provinces of mostly different ages. The references for mineralization ages are given in the text.

sedimentary sequences (Payne et al., 2006; Fanning et al., 2007; Payne et al., 2009; Howard et al., 2011a, b; Szpunar et al., 2011; Reid and Hand, 2012; Armit et al., 2017). During this period the Mount Isa Province in the NAC experienced a similar tectonic history, with *c.* 1.85 Ga inferred arc-related magmatism (McDonald et al., 1997; Bierlein et al., 2008) followed by the deposition of a number of volcanoclastic sedimentary sequences (Jackson et al., 2000; Neumann et al., 2006; Foster and Austin, 2008; Olierook et al., 2022). Wyborn et al. (1987) noted strong geochemical affinities at *c.* 1.79–1.77 Ga volcanic sequences of the Bottletree and Argylla formations in the Mount Isa Province, with the Tidnamurkuna Volcanics in the Peake and Denison Domain and the Myola Volcanics in the Gawler Craton, leading to interpretations that these volcaniclastic sequences formed in a single linear belt (Giles et al., 2004; Betts et al., 2015). This prolonged extensional phase associated with widespread basin development and sedimentation across the NAC and SAC was terminated by the *c.* 1.73–1.69 Ga Kimban Orogeny in the Gawler Craton (Fanning et al., 2007; Hand et al., 2007; Dutch et al., 2008) and the *c.* 1.75–1.71 Ga Wonga Orogeny in the Mount Isa Province (Spence et al., 2022). Both of these orogenic systems were associated with significant magmatism (Fanning et al., 2007; Hand et al., 2007; Neumann et al., 2009).

An extensive rift basin system preserved across the southeastern Gawler Craton and the Curnamona Province in the SAC developed between 1.72 Ga and 1.64 Ga (Conor and Preiss, 2008; Stevens et al., 2008), which coincides with the timing of rift basin development and sedimentation in the Mount Isa Province (Foster and Austin, 2008; Olierook et al., 2022). These sedimentary basins also host giant *syn*-sedimentary Ag-Pb-Zn deposits in both the Curnamona and Mount Isa provinces, interpreted to have formed at *c.* 1685–1650 Ma (Page and Sweet, 1998; Page et al., 2005). During the latest Palaeoproterozoic and early-Mesoproterozoic, the Gawler Craton and Curnamona Province experienced a significant tectonothermal event involving voluminous volcanism and magmatism with tectonism between 1.61 Ga and 1.57 Ga (Daly, 1998; Fanning et al., 1988; Hand et al., 2007; Wade et al., 2012). This tectonothermal event is associated with widespread IOCG-U-REE mineralization in the eastern Gawler Craton and Curnamona Province (Hand et al., 2007; Skirrow et al., 2007; Sawyer et al., 2017; Skirrow et al., 2018; Reid, 2019). Following these events, the Gawler Craton recorded volumetrically minor magmatism at *c.* 1.56 Ga and *c.* 1.51 Ga in the southern Gawler Craton (Fanning et al., 2007; Jagodzinski et al., 2007; Reid et al., 2022) and metamorphism in the northern Gawler Craton at *c.* 1.52 Ga (Reid et al., 2014). In the Mount Isa Province, this period coincides with the first phase (D_1) of the Isan Orogeny between 1.6 Ga and 1.57 Ga, which is largely amagmatic and associated with mineralization in a small number of the IOCG-U-REE deposits (Betts et al., 2006; Duncan et al., 2011; Gauthier et al., 2001; Giles et al., 2006). This is followed by the later phases of the Isan Orogeny that are associated with voluminous magmatism of the Williams and Naraku batholiths and more substantial IOCG-U-REE mineralization across the Mount Isa Province at *c.* 1.53–1.49 Ga (Wyborn, 1998; Betts et al., 2006; Giles et al., 2006; Duncan et al., 2011; Spandler et al., 2016).

Palaeomagnetic data suggest the SAC underwent rotation into its current configuration sometime after *c.* 1.59 Ga (Wingate and Evans, 2003; Giles et al., 2004; Payne et al., 2009). The NAC and SAC are considered to have disaggregated during the break-up of Nuna (Giles et al., 2004), which is recorded in Australia by the formation of rift basins, with the deposition of the Roper Group in northern Australia and Cariewerloo Basin in the Gawler Craton, magmatism in the northern Gawler Craton and reactivation of lithospheric-scale shear zones in the Gawler Craton at *c.* 1.5–1.44 Ga (Jackson et al., 1999; Swain et al., 2005; Fraser and Lyons, 2006; Fraser et al., 2012; Beyer et al., 2018; Morrissey et al., 2019). The re-configuration of the SAC and its subsequent amalgamation with the NAC and WAC during the Albany-Fraser and Musgravian orogenies at *c.* 1.3–1.1 Ga is thought to represent the final assembly of Proterozoic Australia into its present configuration (Howard et al., 2015; Tucker et al., 2015).

2.2. The Peake and Denison Domain

The Peake and Denison Domain is situated in the northeastern Gawler Craton (Fig. 1). The region is largely covered by Phanerozoic sedimentary units, but Proterozoic basement is exposed within two main inliers and a number of subordinate inliers (Fig. 2). Underlying the Neoproterozoic sedimentary units are the *c.* 1800–1740 Ma Peake Metamorphics (Ambrose et al., 1981). These are predominantly composed of the Baltucoodna Quartzite along with various calc-silicate and metapelitic sequences that are interbedded with the *c.* 1790–1770 Ma bimodal Tidnamurkuna Volcanics (Ambrose et al., 1981; Fanning et al., 2007) and intruded by the 1787 ± 8 Ma Wirricurrie Granite (Fanning et al., 2007). A younger phase of volcanic activity is recorded by felsic volcanics that are interbedded with iron-rich sediments at Spring Hills (Fig. 2), which are dated at 1740 ± 6 Ma (Fanning et al., 2007). This age possibly coincides with a *c.* 1730 Ma tonalite intrusion from Lagoon Hill (Hopper, 2001). Early Mesoproterozoic magmatism is also recorded at Lagoon Hill in the eastern part of the region (Fig. 2), with a 1555 ± 14 Ma granite and an *c.* 1530 Ma aplitic intrusion interpreted from igneous zircon overgrowths (Fanning et al., 2007). Greenschist- to upper amphibolite-facies metamorphism is recorded in the Peake and Denison Domain along with sillimanite gneisses and locally developed migmatites (Ambrose et al., 1981). Folding and foliations are also recorded within the Peake Metamorphics and Wirricurrie Granite (Ambrose et al., 1981; Hopper, 2001), but the timing of these events are not well constrained. The Neoproterozoic sequences that unconformably overlie these rocks record deformation during the *c.* 515–480 Ma Delamerian Orogeny, which was associated with the intrusion of the *c.* 513 Ma Bungadillina Monzonite (Fig. 2; Foden et al., 2006).

3. Samples

Samples were collected from diamond drillcore from the Peake and Denison Domain to investigate the timing of magmatism, deformation and alteration. The three drillholes sampled in this study occur approximately 25 km east of the nearest outcropping pre-Neoproterozoic rocks in the Spring Hills and Mount Charles inliers within a broad (~50 km × 80 km) magnetic high that shows prominent fabrics in magnetic imagery (Fig. 2). These drillholes were selected as they provide examples of hydrothermal alteration and mineralization. In the section below a brief summary of each drillhole is provided, followed by the descriptions of samples taken from each drillhole. The drillhole locations and sample details are summarized in Table 1.

3.1. Drillhole DCDH001

DCDH001 targeted a positive gravity anomaly and coincident magnetic high and was drilled to a depth of 404.4 m. The drillhole is dominated by plagioclase-rich felsic gneisses that contain subordinate magnetite and hematite. Numerous biotite-rich intervals and thin granitic veins/pegmatites were also intersected. Anomalous Cu values are distributed throughout this hole, with a notable intercept of 3 m at 2.75% Cu within a magnetite-quartz-biotite breccia at 330–333 m (Ford and Elliston, 1996).

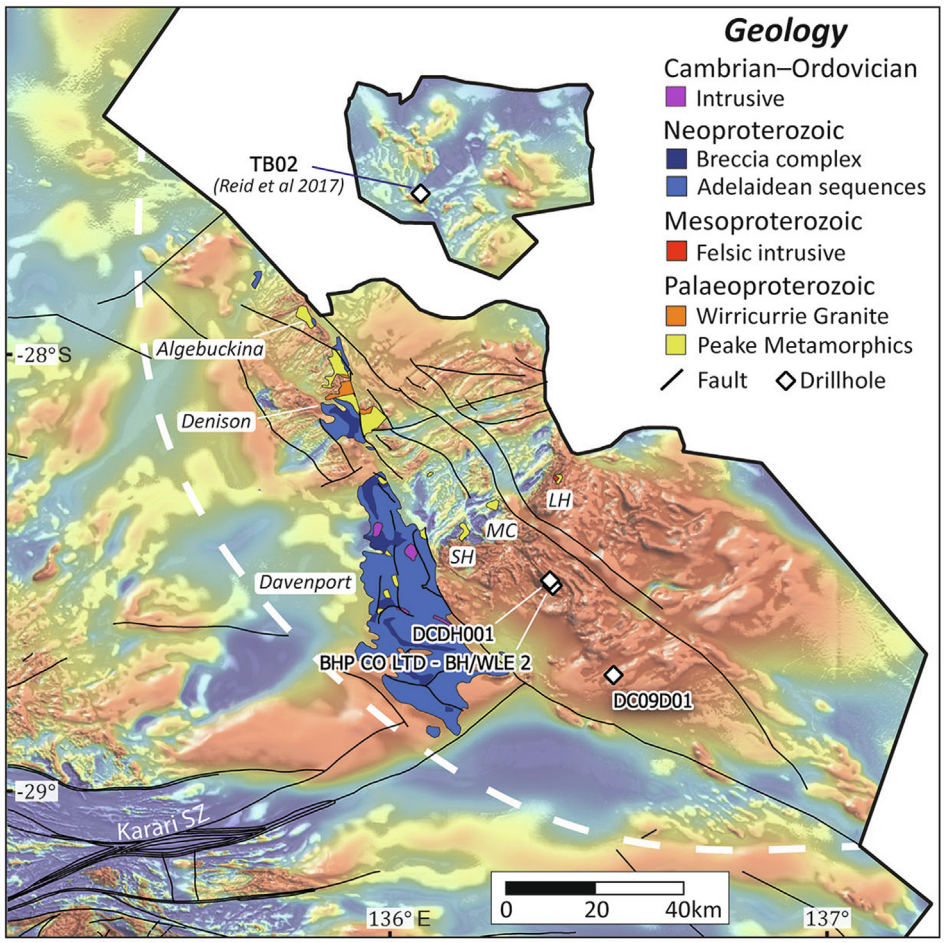

Fig. 2. Exposed Proterozoic and Cambrian–Ordovician rocks of the Peake and Denison Domain superimposed on a TMI (VRTP tilt) and TMI (VRTP) image. The geophysical imagery represents regions covered by Phanerozoic sediments. The drillhole locations for samples from this study and Reid et al. (2017) are shown. Abbreviations for subordinate inliers. SH = Spring Hills, MC = Mount Charles and LH = Lagoon Hill.

Table 1
Synthesis of results. Sample locations are provided in GDA2020. Mineral abbreviations: cpx = clinopyroxene, act = actinolite, ep = epidote, bi = biotite, chl = chlorite, cal = calcite, pl = plagioclase, ttn = titanite, mag = magnetite, ilm = ilmenite.

Drillhole	Lat	Long	Sample	Depth	Lithology	Age	Mineral	Age type
DCDH001	28.51°S	136.36°E	R2509356	350.2 m	Mag-bi breccia	*c.* 490 Ma	Titanite	Alteration
			R2509358	338.1 m	Foliated granitoid	1737 ± 6 Ma	Zircon	Magmatic
						1497 ± 10 Ma	Zircon	Metamorphic
						1487 ± 14 Ma	Titanite	Metamorphic
						1465 ± 12 Ma	Titanite	Alteration
			R2509359	304.6 m	Post-deformation granitoid	1466 ± 12 Ma	Zircon	Magmatic
BHP CO LTD - BH/WLE 2	28.52°S	136.36°E	R2509354	187.3 m	Ttn-ep-chl altered pegmatite	1469 ± 11 Ma	Titanite	Alteration
DC09D01	28.73°S	136.51°E	R2509350	472.5 m	Cpx-ep-act-pl metasomatite	1565 ± 6 Ma	Titanite	Alteration
			R2509351	493.7 m	Act-cal-ep altered pegmatite	1532 ± 8 Ma	Titanite	Alteration
			R2509352 (host)	515.4 m	Cpx-act-ep-pl metasomatite	1519 ± 8 Ma	Titanite	Alteration
			R2509352 (vein)		Ilm-cpx-cal-ep-ttn vein	1494 ± 6 Ma	Titanite	Alteration
			R2509353	518 m	Ep-act-pl altered gneiss	1515 ± 7 Ma	Titanite	Alteration

3.1.1. R2509358

Sample R2509358 is a foliated porphyritic granitoid taken from drillhole DC09D01 at 338.1 m depth (Fig. 3a). It contains K-feldspar, quartz, plagioclase, magnetite and titanite, with minor chlorite, pyrite and chalcopyrite. K-feldspar, quartz and plagioclase grains at 200–400 μm largely dominate the matrix, along with disseminated magnetite grains (50–400 μm). K-feldspar (largely of 4–8 mm) and quartz (up to 2 mm) phenocrysts occur within the matrix, where they may be elongate parallel to the foliation, along with magnetite (Fig. 4a). Titanite grains (largely of 50–300 μm) occur on the margins of magnetite and in the quartzofeldspathic matrix. Titanite grains that occur on the margins of magnetite are typically pale with weak pleochroism, whereas titanite in the matrix in the vicinity of chlorite alteration typically

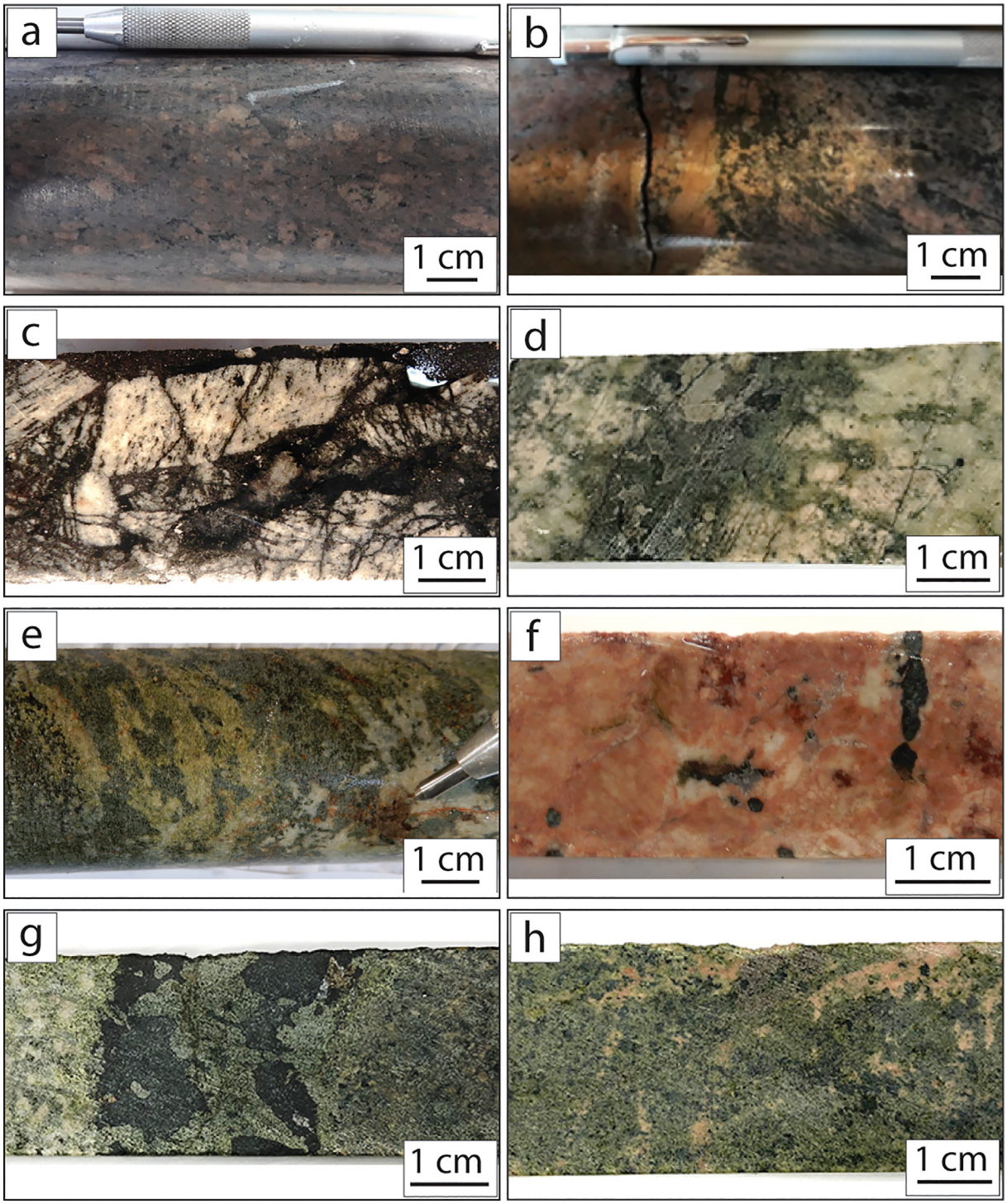

Fig. 3. (a) Elongated phenocrysts in R2509358 showing the foliation. (b) Undeformed felsic intrusive sample R2509359 (left) cross-cutting the foliation. (c) Felsic gneiss clasts in magnetite-biotite breccia matrix from R2509356. (d) Chlorite-alteration in R2509354. (e) Epidote-actinolite-plagioclase alteration with large titanite grain in R2509350. (f) Actinolite alteration in K-feldspar-dominated pegmatite sample R2509351. (g) Ilmenite-dominated vein cross-cutting actinolite-epidote-plagioclase altered host rock in R2509352. (h) Actinolite-epidote alteration in R2509353.

form more rounded grains that show stronger pleochroism from pale to medium brown. Pyrite is disseminated throughout the sample, forming cubic grains that are largely at 150–200 μm.

3.1.2. R2509359

Sample R2509358 is an unfoliated granitoid dyke taken from drillhole DC09D01 at 304.6 m depth. The ~ 1 m wide undeformed dyke represents the last phase of magmatism present in this drillhole as it crosscuts the foliation at a high angle (Fig. 3b). It contains K-feldspar, quartz, plagioclase, magnetite, biotite, titanite, chlorite and minor pyrite. K-feldspar, quartz and plagioclase grains are largely at 0.5–2 mm and constitute ~98% of the rock. Magnetite, biotite and titanite generally occur together in unoriented clusters, forming euhedral to subhedral grains that are largely at 100–500 μm (Fig. 4b). Pyrite (50–200 μm) and chalcopyrite (<10 μm) are disseminated throughout the sample.

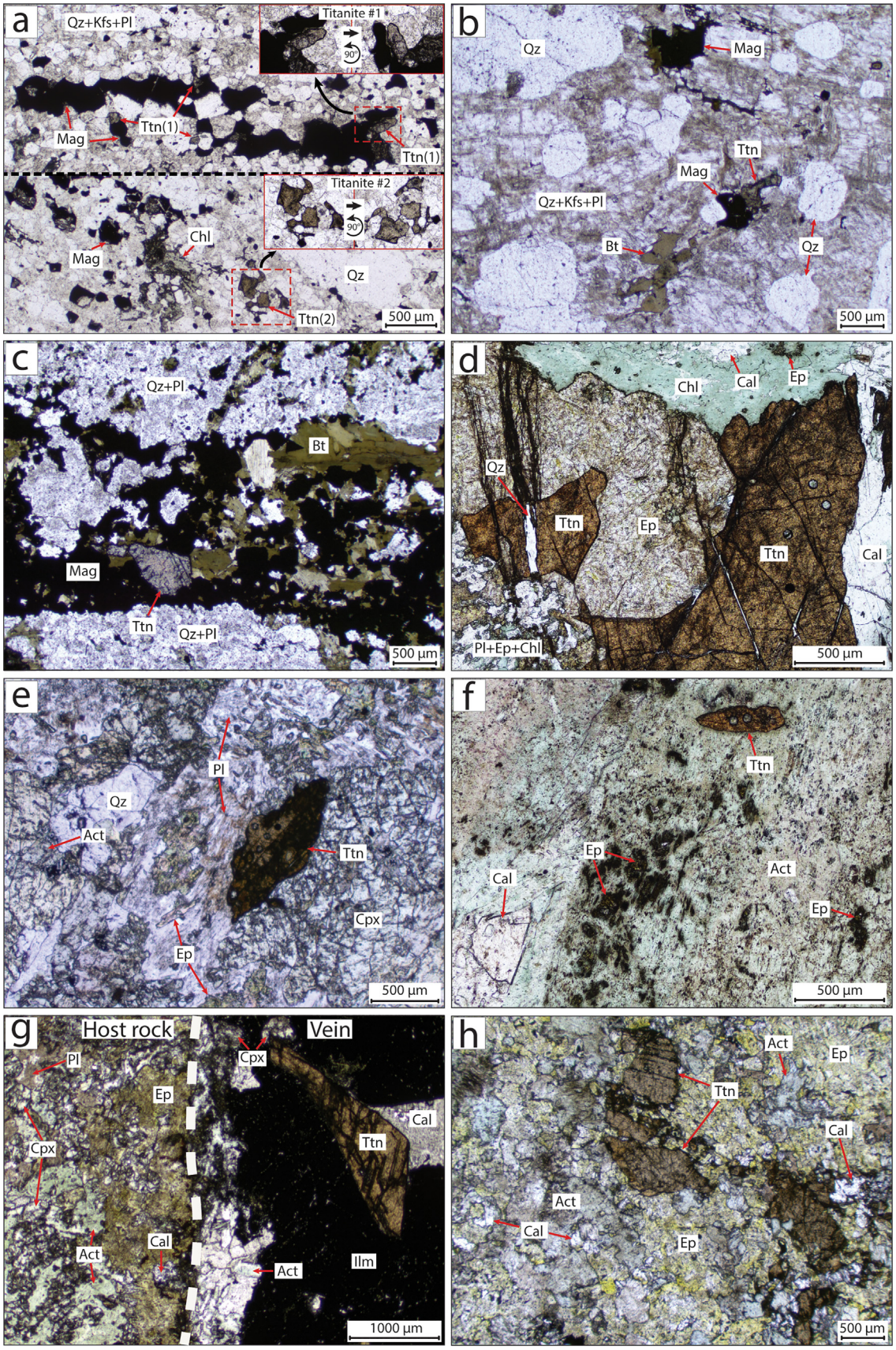

Fig. 4. (a) Microstructural context and different pleochroic properties of the two populations of titanite in R2509358. Titanite #1 (top image) forms grains with low pleochroism that occur at the margins of magnetite that defines the foliation, whereas titanite #2 (bottom image) forms grains with higher pleochroism that occur near chlorite alteration. (b) Unfoliated felsic intrusive sample R2509359. (c) Titanite forming with magnetite, biotite and quartz within the breccia matrix in R2509356. (d) Large titanite grains associated with chlorite, epidote and calcite alteration in R2509354. (e) Slightly altered titanite grain within clinopyroxene-epidote-plagioclase alteration in R2509350. (f) Titanite associated with actinolite-epidote-calcite alteration in R2509351. (g) Interface between the clinopyroxene-epidote-actinolite altered host rock and ilmenite-clinopyroxene-calcite dominated vein in R2509352. (h) Titanite associated with epidote-actinolite and calcite alteration in R2509353.

3.1.3. R2509356

Sample R2509356 is a brecciated felsic gneiss taken from drillhole DCDH001 at 350.20 m depth. It contains quartz, plagioclase, magnetite, biotite and titanite. The felsic gneiss forms angular clasts largely at 2–4 cm that are composed of quartz and plagioclase generally at 200–500 μm, and magnetite grains up to 100 μm (Fig. 3c). The matrix of the breccia is composed of unoriented euhedral biotite grains up to 2 mm, euhedral to subhedral magnetite largely between 100 μm and 400 μm, subhedral titanite grains (up to 1 mm) and minor quartz (Fig. 4c). There is no pyrite or chalcopyrite mineralization in this sample.

3.2. Drillhole BHP CO LTD - BH/WLE 2

BHP CO LTD - BH/WLE 2 sits only ~ 1.5 km SE of DCDH001 as it was targeted at the same positive gravity anomaly and coincident magnetic high. This drillhole was drilled to a depth of 208.9 m and largely contains epidote-chlorite altered amphibolites and quartz-plagioclase-magnetite micro-gneisses.

3.2.1. R2509354

Sample R2509354 is an altered anorthosite pegmatite taken from drillhole BHP CO LTD - BH/WLE 2 at 187.3 m depth. The pegmatite host is dominated by coarse grained plagioclase (up to 1 cm) and is absent of quartz or other feldspars, suggesting the rock is of mafic composition. The pegmatite is altered by epidote, plagioclase, titanite, calcite, chlorite and anatase. Titanite grains vary in size from 0.1 mm to 1 cm and show variable degrees of alteration to anatase and exsolution of ilmenite along cleavage planes. Epidote generally occurs as small grains (<50 μm) that form in clusters, or are intergrown with fine-grained plagioclase, chlorite and calcite. These minerals are overprinted by a set of < 50 μm wide veinlets calcite or quartz (Fig. 4d).

3.3. Drillhole DC09D01

Sample DC09D01 targeted a large (~15 km × 2.5 km) arcuate positive gravity anomaly ~ 25 km to the SE of the previous two drillholes and was drilled to 618.8 m depth. Beneath 395 m of Cretaceous sediments, the basement is composed of interlayered metasedimentary gneisses that show intense calc-silicate alteration. Amphibole and epidote are the dominant alteration minerals, with locally present hematite and K-feldspar alteration. A series of pegmatites were also intersected, with some containing trace amounts of pyrite, but no significant mineralization.

3.3.1. R2509350

Sample R2509350 is a calc-silicate metasomatite taken from drillhole DC09D01 at 472.5 m depth (Fig. 3e). It contains clinopyroxene, epidote, plagioclase, actinolite, quartz, calcite, titanite and magnetite. Clinopyroxene, epidote, plagioclase and actinolite are intergrown and represent the dominant alteration minerals in this sample, forming grains largely at 1–10 mm. Magnetite, calcite and titanite are less abundant in the alteration assemblage, with magnetite and calcite forming grains at 100–500 μm and titanite forming grains of variable size largely at 0.1–1 mm. Titanite grains commonly have dark margins in plane-polarised light (Fig. 4e), which suggests they have experienced minor alteration.

3.3.2. R2509351

Sample R2509351 is an altered pegmatite taken from drillhole DC09D01 at 493.7 m depth. It contains K-feldspar, quartz, plagioclase, actinolite, calcite, epidote and titanite (Fig. 3f). The pegmatite is dominated by K-feldspar, and also contains quartz and plagioclase that form grains up to 500 μm. The pegmatite is altered by large grains (up to 1 cm) of actinolite that contain small inclusions (<50 μm) of epidote that appear to be altered with dark haloes around the grains (Fig. 4f). Calcite (up to 500 μm) and titanite (100–500 μm) are also associated with the alteration assemblage, forming as inclusions within and at the margins of actinolite.

3.3.3. R2509352

Sample R2509352 is a calc-silicate metasomatite taken from drillhole DC09D01 at 515.4 m depth. The sample is a strongly altered host rock crosscut by a ~3 cm-wide vein dominated by ilmenite (Fig. 3g). The host rock contains clinopyroxene, actinolite, epidote, plagioclase, hornblende, quartz and titanite, and the cross-cutting vein comprises ilmenite, clinopyroxene, actinolite, epidote, calcite and titanite. Ilmenite and clinopyroxene are the most dominant minerals within the vein, forming grains up to 1.5 cm that are associated with calcite, actinolite and euhedral titanite grains that are up to 3 mm (Fig. 4g). Epidote (up to 500 μm) commonly forms on the edges of ilmenite and titanite within the vein. Epidote is most abundant at the contact between the host rock and the cross-cutting vein (Fig. 4g). There are also variations in the abundance of clinopyroxene, amphibole and plagioclase throughout the host rock. Actinolite is the dominant amphibole in the host rock, but hornblende is present in some domains. Actinolite inclusions occur within clinopyroxene, but actinolite and hornblende are also observed pseudomorphing clinopyroxene, suggesting multiple generations of amphibole are present. The variations in mineralogy in the host rock appear to be spatially controlled but do not seem to correspond to distance from the vein and therefore may reflect protolithic variation. Titanite is also disseminated throughout the host rock, forming smaller and more anhedral grains that are generally at 100–300 μm.

3.3.4. R2509353

Sample R2509353 is a calc-silicate metasomatite taken from drillhole DC09D01 at 518 m depth. This sample was taken approximately 2.5 m downhole from Sample R2509352 to investigate the age and composition of titanite in the country rock at a greater distance from the ilmenite-rich vein. This sample has a similar alteration assemblage to the host rock of R2509352, containing epidote, actinolite, K-feldspar, calcite, titanite, clinopyroxene, ilmenite and pyrite (Fig. 3h). Epidote, actinolite and K-feldspar are the dominant alteration minerals in the sample, forming grains typically at 0.5–1 mm that are intergrown. Clinopyroxene is less abundant and is seen being pseudomorphed by actinolite. Titanite grains are largely of 50–300 μm and are commonly associated with calcite (Fig. 4h). Minor pyrite is disseminated throughout the sample, forming irregular shaped grains at 50–300 μm.

4. Methods

U–Pb geochronology of zircon and titanite was undertaken using Laser Ablation–Inductively Coupled Plasma Mass Spectrometry (LA-ICP-MS), using a Resolution LR 193-nm Excimer laser coupled to an Agilent 7900x Quadrupole ICP-MS at Adelaide Microscopy, University of Adelaide. Prior to LA-ICP-MS analysis, grains were imaged using a FEI Quanta 600 MLA Scanning Electron Microscope (SEM) at Adelaide Microscopy to identify target zones to analyse. Zircon grains were imaged using a Gatan Cathodoluminescence (CL) detector attached to the SEM, and back-scattered electron (BSE) images were collected for titanite.

Zircon analyses involved sequential measurement on masses ^{202}Hg, ^{204}Pb, ^{206}Pb, ^{207}Pb, ^{232}Th and ^{238}U for dwell times of 20 ms, 20 ms, 30 ms, 60 ms, 20 ms, 20 ms and 30 ms, respectively. Zircon grains were ablated with a frequency of 5 Hz, intensity of 2 J/cm^2 and a spot size of 30 μm. The acquisition time of each analysis was 60 s, comprising 30 s of background measurement and

30 s of ablation. Zircon data were corrected for mass bias, elemental fractionation and instrument drift based on the measured isotopic ratios of the primary zircon reference, GJ-1 (TIMS normalisation data: $^{207}Pb/^{206}Pb$ = 608.3 Ma, $^{206}Pb/^{238}U$ = 600.7 Ma, $^{207}Pb/^{235}U$ = 602.2 Ma; Jackson et al., 2004). Secondary reference standards Plesovice and 91500 were analysed concurrently to measure data accuracy by standard–sample bracketing every ~ 15 unknown analyses. Throughout the analytical session, Plesovice and 91,500 yielded respective weighted mean ages of $^{206}Pb/^{238}U$ = 337.7 ± 1.9 Ma (MSWD = 1.3, n = 9), and $^{207}Pb/^{206}Pb$ = 1073 ± 28 Ma (MSWD = 1.7, n = 7), respectively. Both ages are within uncertainty of the published values for the standards (Wiedenbeck et al., 1995; Sláma et al., 2008).

Titanite geochronology was largely performed *in-situ* from thin sections (except for R2509358), and additional compositional data were collected during analysis. Analyses involved sequential measurement on masses ^{202}Hg, ^{204}Pb, ^{206}Pb, ^{207}Pb, ^{208}Pb, ^{232}Th and ^{238}U for dwell times of 20 ms, 20 ms, 30 ms, 60 ms, 20 ms, 20 ms and 30 ms, respectively. Trace elements ^{51}V, ^{53}Cr, ^{90}Zr, ^{93}Nb, ^{139}La, ^{140}Ce, ^{141}Pr, ^{146}Nd, ^{147}Sm, ^{153}Eu, ^{157}Gd, ^{159}Tb, ^{163}Dy, ^{165}Hm, ^{166}Er, ^{169}Tm, ^{172}Yb, ^{175}Lu and ^{181}Ta each had dwell times of 10 ms and ^{29}Si, ^{43}Ca, ^{47}Ti, ^{55}Mn and ^{57}Fe each had dwell times of 5 ms. Titanite grains were ablated with a frequency of 5 Hz, intensity of 3.5 J/cm^2 and a spot size of 50 μm. The acquisition time of each analysis was 80 s, comprising 30 s of background measurement and 50 s of ablation. Titanite U–Pb data were corrected for mass bias, elemental fractionation and instrument drift based on the measured isotopic ratios of the primary titanite reference, MKED-1 (TIMS normalization data: $^{207}Pb/^{206}Pb$ age = 1521.02 ± 0.55 Ma; Spandler et al., 2016). Titanite compositional data were corrected using the standard reference material NIST610 (Jochum et al., 2011). A large titanite grain ARK was analysed concurrently as a secondary standard to measure data accuracy by standard–sample bracketing every ~15 unknown analyses. Throughout three analytical sessions, ARK yielded a weighted mean $^{206}Pb/^{238}U$ age of 439 ± 1 Ma (n = 58, MSWD = 1.07). This is within uncertainty of the published ID-TIMS age of 437.6 ± 3.6 Ma from Elburg et al. (2003).

Zircon data were processed using Iolite software (version 3.65, Paton et al., 2011) and titanite data were processed using LADR software (version 1.1.06, Norris and Danyushevsky, 2018). All age data were plotted using IsoplotR (Vermeesch, 2018). Ages were not corrected for common Pb due to isobaric interference by ^{204}Hg present in the Ar–He carrier gas. The quoted analytical uncertainties on individual analyses include contributions from the external reproducibility of the primary reference standards and are given at 2σ level. Uncertainties quoted with weighted mean and upper intercept calculations are given at the 95% confidence level.

5. Results

Zircon ages are calculated using weighted mean $^{207}Pb/^{206}Pb$ calculations from analyses within 2σ uncertainty of concordia, or upper intercepts from concordant and discordant data. Titanite ages are determined using weighted mean age calculations from analyses within 2σ uncertainty of concordia, and compositional data are also used where appropriate to distinguish populations and aid geochronological interpretations. Due to titanite having a greater propensity to incorporate non-radiogenic Pb during formation, $^{206}Pb/^{204}Pb$ ratios (corrected against NIST 610) are used to infer the influence of non-radiogenic Pb on titanite ages in each sample. A $^{206}Pb/^{204}Pb$ threshold value of 5000 is used to filter titanite ages. This effectively removes data from age calculations that may deviate from the true age by >0.4% as a result of the incorporation of non-radiogenic Pb (e.g. Gehrels et al., 2008). However, as the isobaric ^{204}Hg interference reduces the reliability of the ^{204}Pb data, it may be the case that some influence of non-radiogenic Pb is present within analyses that have $^{206}Pb/^{204}Pb$ values below this threshold. Therefore, in samples where non-radiogenic Pb appears to influence the titanite age data (i.e. concordant but deflected toward higher $^{207}Pb/^{206}Pb$ values), $^{206}Pb/^{238}U$ ages are preferentially used to reduce the possible influence of non-radiogenic Pb contamination.

The U–Pb age data from zircon and titanite grains (Fig. 5) are presented on concordia diagrams and weighted mean age plots presented in Fig. 6. Titanite REE data are presented on chondrite normalised REE diagrams in Fig. 7. Concordant analyses with $^{206}Pb/^{204}Pb$ ratios < 5000 are included on weighted mean plots to demonstrate the influence of non-radiogenic Pb on the age distribution, but are not included in the age calculations. All LA-ICP-MS data from zircon and titanite are presented in Supplementary Data Table S1. Weighted mean plots and age calculations for titanite with all data included are presented in Supplementary Data Fig. S1 to allow comparison with the final quoted age for each sample.

5.1. R2509358

Zircon grains from this sample are mostly euhedral and show magmatic oscillatory zoning that is variably overprinted by resorption and/or recrystallisation features. Grains range of 100–300 μm in length, with typical aspect ratios of 2:1 to 4:1. CL imagery (Fig. 5a) shows most grains have dark rims surrounding the magmatic core with rims up to 100 μm thick at the terminus of the grain. One of the analysed grains has a low CL response for the entire grain and is interpreted to be wholly metamorphic or grew during alteration.

Thirty-one analyses were undertaken on twenty-nine zircon grains, with twenty-six analyses yielding signals that were of suitable quality to determine an age for the analysis. Analyses from the zircon cores yield an upper intercept age and weighted mean age that are in agreement and therefore considered reliable ages. The upper intercept age is 1739 ± 7 Ma (n = 22, MSWD = 1.5; Fig. 6a), while a weighted mean $^{207}Pb/^{206}Pb$ age calculation of concordant analyses yields an age of 1737 ± 6 Ma (n = 18, MSWD = 0.92). The lower intercept age of 277 ± 47 Ma suggests that there has been some ancient resetting of the zircon cores during a Phanerozoic event. Four analyses were also undertaken on low CL response grains or rims, yielding a weighted mean $^{207}Pb/^{206}Pb$ age of 1497 ± 12 Ma (MSWD = 0.47; Fig. 6a).

Titanite grains from this sample were analysed in a grain mount and record distinct variations in brightness in BSE images. The darker grains in BSE are slightly larger (150–200 μm) on average and typically have straight edges, whereas the brighter grains are largely at 100–150 μm with rounded edges. Both forms of titanite show patchy zoning in BSE images (Fig. 5b). A total of twenty analyses were collected from this sample and confirm two chemically distinct titanite populations.

Eleven analyses from the darker grains have comparatively low REE concentrations that show negative trends in the light rare earth elements (LREEs) between La–Sm, mostly positive Eu anomalies (except for three analyses that are slightly negative), and slightly concave trends in heavy rare earth elements (HREEs) between Gd–Lu (Fig. 7a). These analyses also correspond to average concentrations of: Fe = 9763 ppm, Nb = 461 ppm, Ta = 16 ppm, Th = 322 ppm, U = 55 ppm. The Th/U ratios are of 4.3–8.6, with an average of 5.9. All eleven analyses collected from this population are concordant with insignificant levels of non-radiogenic Pb. They yield a weighted mean $^{206}Pb/^{238}U$ age of 1485 ± 16 Ma (MSWD = 2.11) and a weighted mean $^{207}Pb/^{206}Pb$ age of 1493 ± 22 Ma (MSWD = 2.11). Non-radiogenic Pb is not significant in this sample and therefore a $^{207}Pb/^{206}Pb$ age is consid-

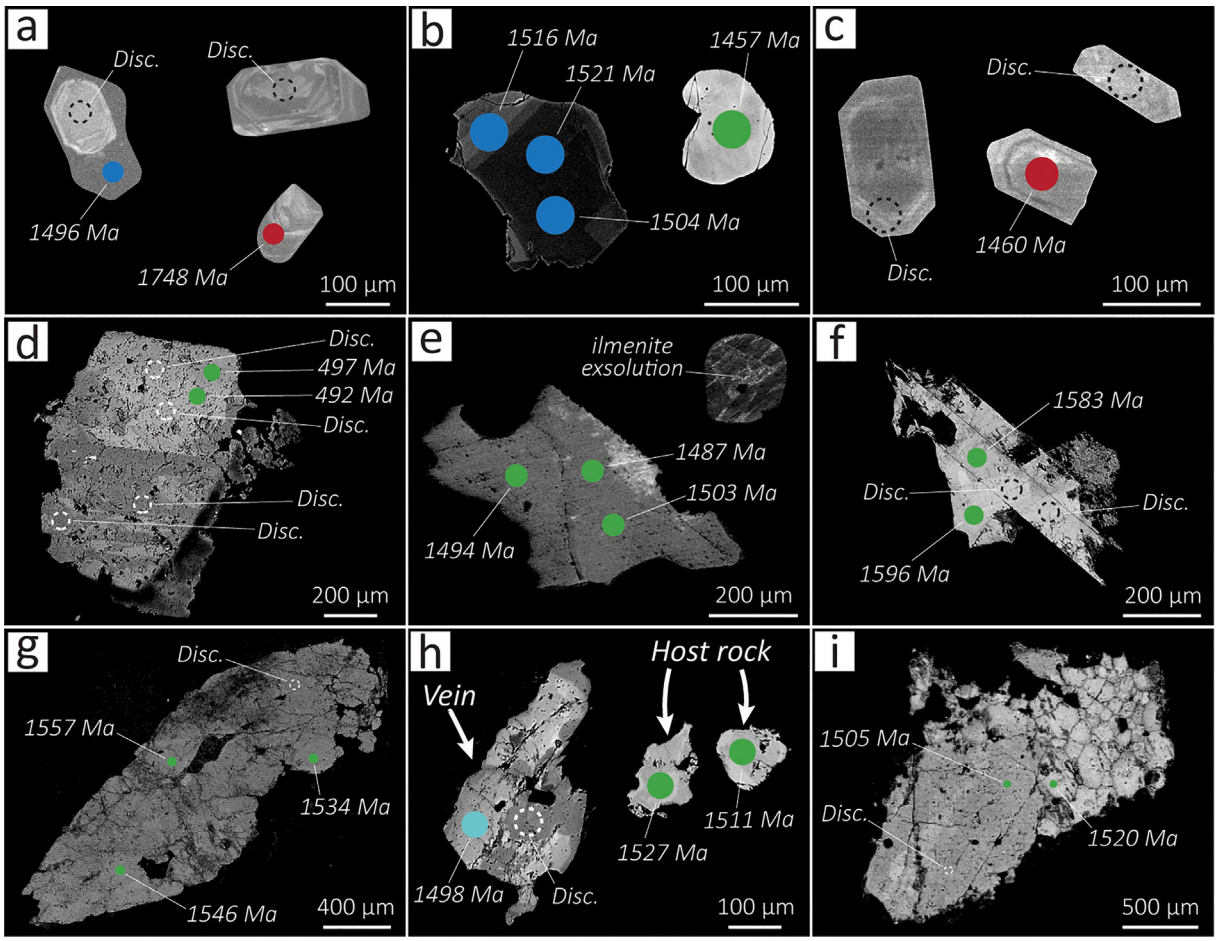

Fig. 5. Zircon CL and titanite BSE images. (a) Magmatic zircon cores and low CL response rims from R2509358. (b) Representative titanite grains from the two populations in R2509358. The low CL response grain represents low REE and Fe concentrations which is inferred as titanite generation #1 in Fig. 4a, whereas the high CL response grain represents high REE and Fe concentrations which is inferred as titanite generation #2 in Fig. 4a (see in text). (c) Sample R2509359 zircon. (d) Sample R2509356 titanite. (e) Sample R2509354 titanite. (f) Sample R2509350 titanite. (g) Sample R2509351 titanite. (h) Representative titanite grains from the altered host rock and vein in Sample R2509352. (i) Sample R2509353 titanite.

ered reliable; however, an MSWD of 2.11 indicates this $^{207}Pb/^{206}Pb$ age is not statistically meaningful. Excluding the oldest age of 1575 Ma yields a weighted mean $^{207}Pb/^{206}Pb$ age of 1487 ± 14 Ma (n = 10, MSWD = 1.28; Fig. 6b) for this population.

Nine analyses from the brighter grains in BSE images have comparatively high REE concentrations that show slight convex trends in LREEs between La–Sm, consistently strong negative Eu anomalies and largely flat trends in HREEs (Fig. 7a). These analyses also correspond to average concentrations of: Fe = 20,484 ppm, Nb = 5983 ppm, Ta = 805 ppm, Th = 441 ppm, U = 198 ppm. The Th/U ratio is of 1.6–2.7, with an average of 2.19. All nine analyses collected from this population are concordant, but one analysis with significant non-radiogenic Pb was excluded from age calculations. The remaining eight analyses yield a weighted mean $^{206}Pb/^{238}U$ age of 1472 ± 19 Ma (MSWD = 2.46) and a weighted mean $^{207}Pb/^{206}Pb$ age of 1465 ± 12 Ma (MSWD = 0.68; Fig. 6b). As the data are concordant and the $^{206}Pb/^{238}U$ and $^{207}Pb/^{206}Pb$ ages are in agreeance the impact of non-radiogenic Pb is considered to be negligible, and the statistically coherent weighted mean $^{207}Pb/^{206}Pb$ age is considered reliable.

5.2. R2509359

Zircon grains from this sample are 75–300 µm in length with aspect ratios between 1:1 and 5:1; however, most crystals have a ratio around 3:1. The grains are dominantly very low CL response with internal textures that are considered a mixture of relict oscillatory zoning and metamictisation (Fig. 5c). One grain includes a bright CL response core. The low CL response of the remaining grains limits the detail that can be obtained from the imaging.

Twenty-two analyses were attempted on twenty-one grains for this sample. The analytical signals were of relatively poor quality (e.g. inclusions, variable Pb-loss and/or common Pb) and hence only seventeen analyses yielded usable data. One analysis was on the bright CL response core and this yielded a $^{207}Pb/^{206}Pb$ age of 1727 ± 32 Ma. The remaining analyses yield upper and lower intercepts of 1448 ± 31 Ma and 494 ± 192 Ma but with an MSWD of 5.9 indicating the ages are not statistically reliable (Fig. 6c). Using only ages from the upper grouping of concordant analyses yields a weighted mean $^{207}Pb/^{206}Pb$ age of 1466 ± 12 Ma (Fig. 6c; MSWD = 0.54, n = 4).

5.3. R2509356

Titanite grains analysed from this sample are between 0.2 mm and 1 mm and occur within the matrix of the breccia, where they typically form adjacent to magnetite grains. The titanite grains are pitted and show patchy zoning in BSE images (Fig. 5d). A total of twenty-four titanite analyses were collected and have relatively coherent REE compositions. The titanite grains have low LREE con-

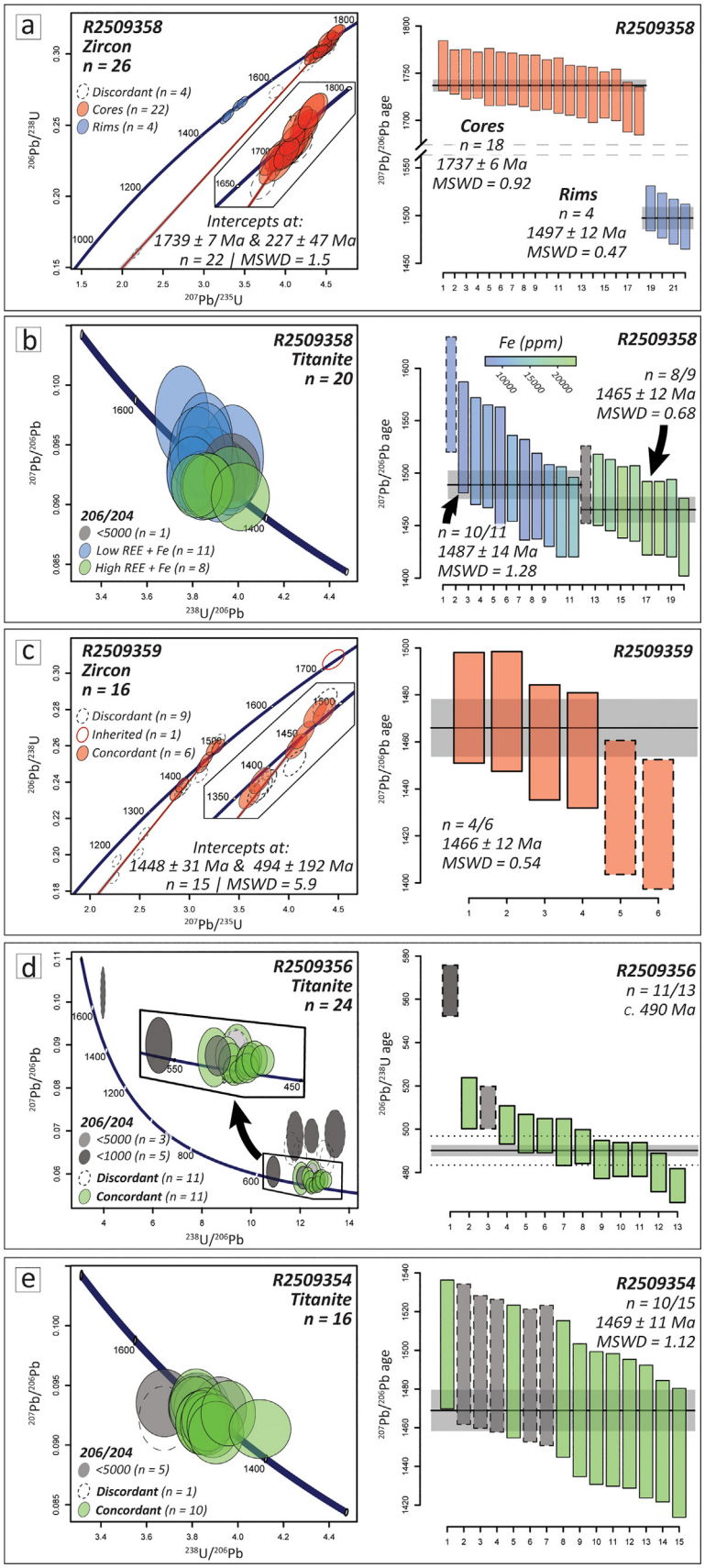

Fig. 6. Concordia diagrams and weighted mean plots for zircon and titanite. Grey analyses indicate high $^{206}Pb/^{204}Pb$ values that are excluded from age calculations due to non-radiogenic Pb contamination. Error bars on weighted mean plots are presented as 2σ and ages with dashed margins were excluded from age calculations. (a) Sample R2509358 zircon with weighted mean $^{207}Pb/^{206}Pb$ age plot. (b) Sample R2509358 titanite with weighted mean $^{207}Pb/^{206}Pb$ age plot coloured for Fe concentration. (c) Sample R2509359 zircon with weighted mean $^{207}Pb/^{206}Pb$ age plot. (d) Sample R2509356 titanite with weighted mean $^{206}Pb/^{238}U$ age plot. (e) Sample R2509354 titanite with weighted mean $^{207}Pb/^{206}Pb$ age plot. (f) Sample R2509350 titanite with weighted mean $^{206}Pb/^{238}U$ age plot. (g) Sample R2509351 titanite with weighted mean $^{206}Pb/^{238}U$ age plot. (h) Sample R2509352 titanite with weighted mean $^{206}Pb/^{238}U$ age plot. (i) Sample R2509353 titanite with weighted mean $^{206}Pb/^{238}U$ age plot.

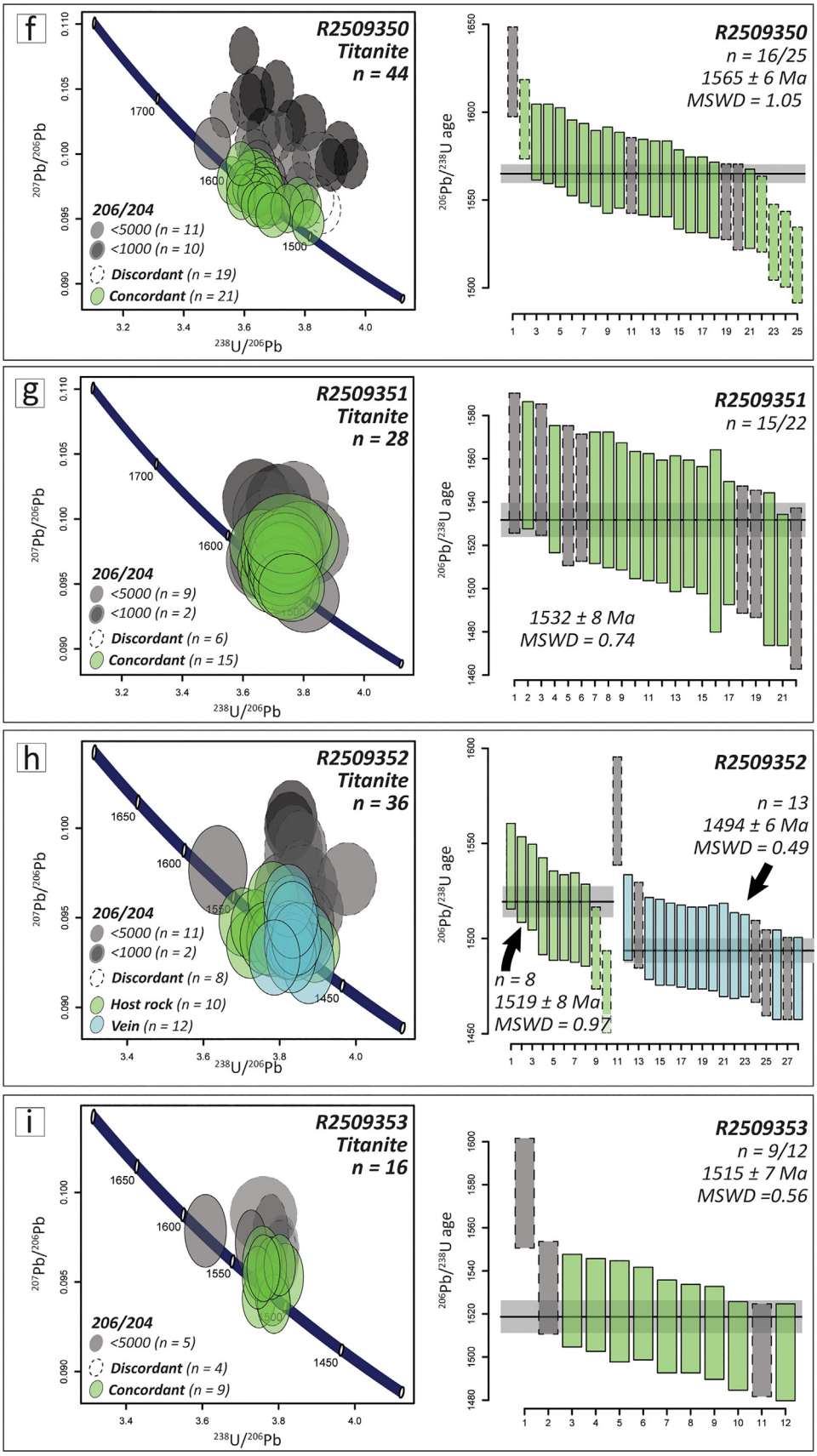

Fig. 6 (*continued*)

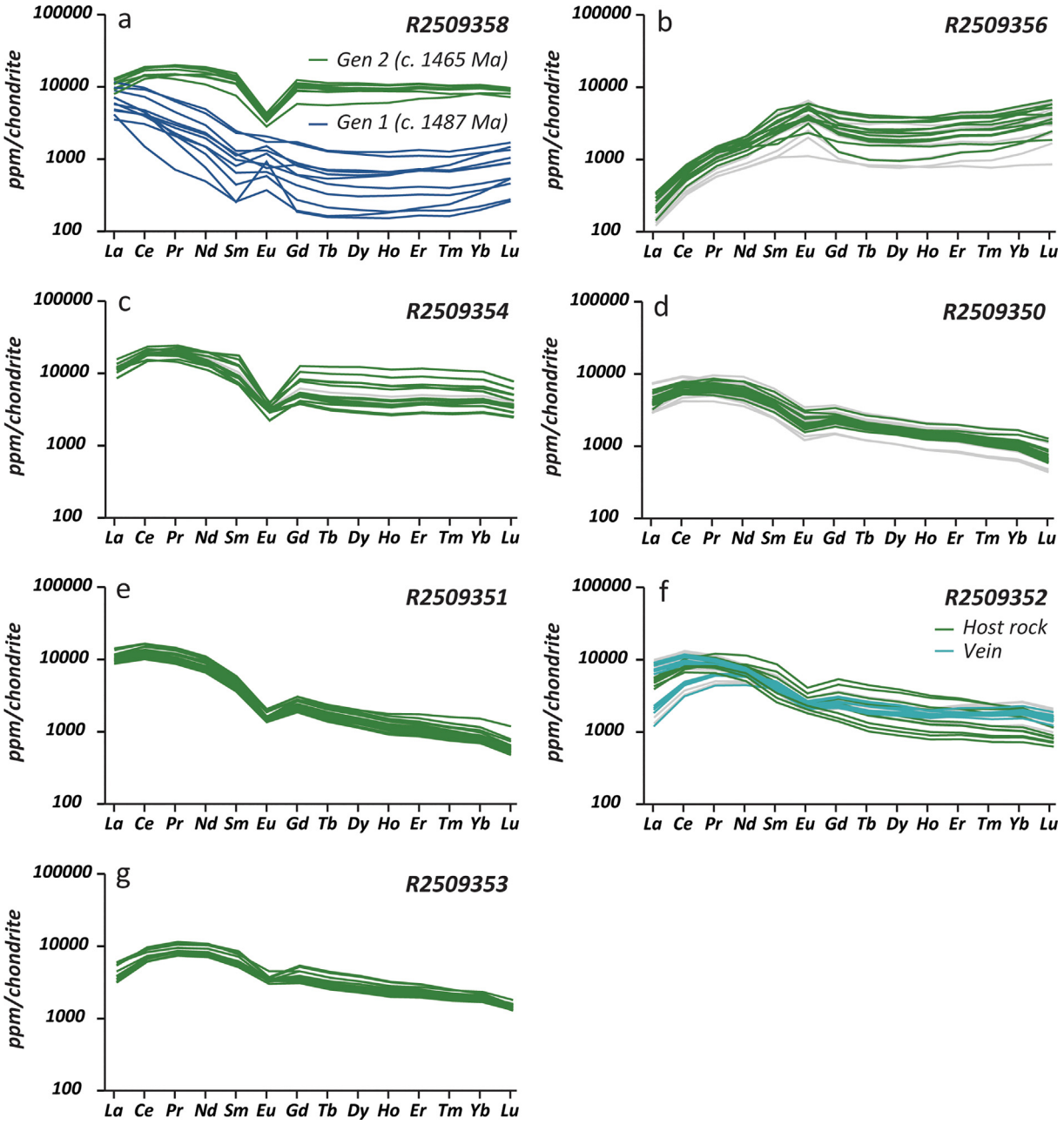

Fig. 7. Chondrite normalised REE plots for titanite. Normalised to the values of McDonough and Sun (1995).

centrations with positive trends from La–Sm, positive Eu anomalies, and slightly concave trends in the HREEs that increase most significantly from Tm–Lu. The HREE concentrations vary considerably between analyses (Fig. 7b), but the overall consistency in REE trends suggests only a single generation of titanite is present in this sample.

Eleven discordant analyses and another two analyses with significant non-radiogenic Pb were excluded from age calculations. The remaining eleven analyses yielded a weighted mean $^{206}Pb/^{238}U$ age of 490 ± 7 Ma (Fig. 6d), but with an MSWD of 5.13 indicating this age is not a coherent population. The ages are spread between *c.* 515 Ma and 475 Ma and show no relationship with REE concentrations. Given this study is focused on the Palaeo- to early-Mesoproterozoic evolution of the region we do not attempt to refine this age further.

5.4. R2509354

Titanite grains analysed from this sample are between 0.2 mm and 1 mm and largely unzoned in BSE images, except for minor alteration on their margins (Fig. 5e). A total of sixteen titanite analyses were collected from this sample. They show consistent REE trends with high LREE concentrations that form convex trends between La–Sm, consistently negative Eu anomalies, and relatively flat HREE slopes. The HREE concentrations vary considerably between analyses (Fig. 7c), but the overall consistency in REE trends suggests only one generation of titanite is present in this sample.

One discordant analysis and another five analyses with significant non-radiogenic Pb were excluded from age calculations, leaving ten analyses that yield a $^{206}Pb/^{238}U$ weighted mean age of

1475 ± 22 Ma (MSWD = 3.60) and a $^{207}Pb/^{206}Pb$ weighted mean age of 1469 ± 11 Ma (MSWD = 1.12; Fig. 6e). An MSWD of 3.60 indicates the $^{206}Pb/^{238}U$ weighted mean age is unreliable and is likely to be influenced by both slight reverse discordance and Pb-loss, despite most analyses remaining within 2σ uncertainty of concordia. The $^{207}Pb/^{206}Pb$ ages in this sample are likely to have some influence from non-radiogenic Pb, with low $^{206}Pb/^{204}Pb$ values dominating the older portion of the $^{207}Pb/^{206}Pb$ ages. Despite this, the weighted mean $^{207}Pb/^{206}Pb$ age is within uncertainty of and slightly younger than the weighted mean $^{206}Pb/^{238}U$ age, suggesting the influence of non-radiogenic Pb is negligible and therefore the weighted mean $^{207}Pb/^{206}Pb$ age is preferred for this sample.

5.5. R2509350

Titanite grains analysed from this sample are between 0.2 mm and 1 mm and show patchy zoning in BSE images (Fig. 5f). A total of forty-four titanite analyses were collected from this sample. They show consistent REE compositions, with high LREE concentrations that form convex trends in LREEs from La–Sm, negative Eu anomalies, and slightly negative trends in HREEs (Fig. 7d). The homogeneity of titanite compositions suggests only one generation of titanite is present within this sample.

Nineteen discordant analyses and four additional analyses with significant non-radiogenic Pb were excluded from age calculations, leaving twenty-one analyses that yield a weighted mean $^{206}Pb/^{238}U$ age of 1558 ± 10 Ma (MSWD = 3.51) and a weighted mean $^{207}Pb/^{206}Pb$ age of 1566 ± 13 Ma (MSWD = 3.69). The MSWD values > 3.50 indicate these ages are not statistically reliable. Non-radiogenic Pb is common in titanite from this sample and appears to influence the $^{207}Pb/^{206}Pb$ ages, with concordant analyses with low $^{206}Pb/^{204}Pb$ ratios prevalent among the older $^{207}Pb/^{206}Pb$ ages and therefore a $^{206}Pb/^{238}U$ age is considered more reliable. Excluding the four youngest ages (1542–1513 Ma) due to recent partial Pb loss and an outlying old age (1596 Ma) yields a weighted mean $^{206}Pb/^{238}U$ age of 1565 ± 6 Ma (n = 16, MSWD = 1.05; Fig. 6f).

5.6. R2509351

Titanite grains analysed from this sample are between 0.4 mm and 3 mm and commonly show pitted textures with patchy zoning in BSE images (Fig. 5g). A total of twenty-eight titanite analyses were collected from this sample. They show consistent REE compositions, with high LREE concentrations that form convex trends from La–Sm, negative Eu anomalies, and slightly negative trends in HREEs (Fig. 7e). The homogeneity of titanite compositions suggests only one generation of titanite is present within this sample.

Six discordant analyses and another seven analyses with significant non-radiogenic Pb were excluded from age calculations, leaving fifteen analyses that yield a weighted mean $^{206}Pb/^{238}U$ age of 1532 ± 8 Ma (MSWD = 0.74; Fig. 6g) and a weighted mean $^{207}Pb/^{206}Pb$ age of 1555 ± 15 Ma (MSWD = 2.20). Non-radiogenic Pb seems to influence the $^{207}Pb/^{206}Pb$ ages in this sample, with low $^{206}Pb/^{204}Pb$ ratios dominating the older $^{207}Pb/^{206}Pb$ ages. Therefore, the statistically coherent $^{206}Pb/^{238}U$ age is considered more reliable for this sample.

5.7. R2509352

Titanite grains were analysed from the altered host rock as well as in a cross-cutting ilmenite-rich vein in this sample. The titanites analysed are between 0.15 mm and 3 mm and commonly show patchy zoning in BSE images regardless of their location (Fig. 5h). A total of thirty-six analyses were collected, with eleven analyses from titanite in the host rock and twenty-five analyses from titanite within the vein.

The titanite grains from the altered host rock show high LREE concentrations that form convex trends from La–Sm and HREEs that vary significantly in concentration between analyses but have consistent negative slopes. Eu anomalies vary from negative to absent, with analyses with no Eu anomaly also having the lowest HREE concentrations (Fig. 7f). The host rock titanite analyses have average elemental concentrations of 633 ppm V, 12,810 ppm Fe, 383 ppm Zr, 1832 ppm Nb, 201 ppm Ta, 385 ppm Th and 226 ppm U. The Th/U ratios are of 1.1–2.1, with an average of 1.7. One discordant analysis from a titanite grain in the host rock population was removed from age calculations, leaving ten analyses that yield a weighted mean $^{206}Pb/^{238}U$ age of 1511 ± 14 Ma (MSWD = 2.83) and a weighted mean $^{207}Pb/^{206}Pb$ age of 1514 ± 8 Ma (MSWD = 1.85). The high MSWD values indicate these ages are not statistically meaningful. As significant levels of non-radiogenic Pb occur within titanite in this sample, a $^{206}Pb/^{238}U$ age is considered more reliable. Removing the two youngest ages (1472 Ma and 1495 Ma) from age calculations due to recent partial Pb-loss yields a weighted mean $^{206}Pb/^{238}U$ age of 1519 ± 8 Ma (n = 8, MSWD = 0.97; Fig. 6h) for titanite in the altered host rock.

Titanite grains within the vein show two distinct REE trends. All have a convex trend in LREEs, with some analyses having similar LREE concentrations to titanite in the host rock, but others have much lower concentrations of La, Ce and Pr. All analyses have negative Eu anomalies and have similar concentrations of HREEs that follow a flat to slightly negative trend. These analyses have average elemental concentrations of 953 ppm V, 17,176 ppm Fe, 199 ppm Zr, 2307 ppm Nb, 355 ppm Ta, 156 ppm Th and 203 ppm U. The Th/U ratios are of 0.54–0.95, with an average of 0.75. Seven discordant analyses and five analyses with significant non-radiogenic Pb were removed from age calculations for the vein-hosted titanite population. The remaining thirteen analyses yield a weighted mean $^{206}Pb/^{238}U$ age of 1494 ± 6 Ma (MSWD = 0.49; Fig. 6h) and a weighted mean $^{207}Pb/^{206}Pb$ age of 1503 ± 12 Ma (MSWD = 2.05). As a large proportion of titanite analyses from this sample contain significant levels of non-radiogenic Pb, the $^{206}Pb/^{238}U$ age is preferred.

5.8. R2509353

Titanite grains analysed from this sample are between 0.15 mm and 2 mm and show pitted textures with patchy zoning in BSE images. Some grains also show signs of alteration at their margins (Fig. 5i). A total of sixteen titanite analyses were collected from this sample. They show consistent REE compositions, with high LREE concentrations that form convex trends from La–Sm, negative Eu anomalies, and slightly negative trends in HREEs (Fig. 7g). The homogeneity of titanite compositions suggest a single generation of titanite is present within this sample.

Four discordant analyses and another three analyses with significant non-radiogenic Pb were excluded from age calculations. The remaining nine analyses yield a $^{206}Pb/^{238}U$ weighted mean age of 1515 ± 7 Ma (MSWD = 0.56; Fig. 6i) and a $^{207}Pb/^{206}Pb$ weighted mean age of 1528 ± 13 Ma (MSWD = 2.18). Non-radiogenic Pb appears to influence the $^{207}Pb/^{206}Pb$ ages, with significant levels recorded in the three oldest concordant ages. Therefore, the statistically coherent $^{206}Pb/^{238}U$ age is considered more reliable.

6. Discussion

6.1. Tectonothermal and hydrothermal evolution of the Peake and Denison Domain

Zircon U–Pb ages from drillhole DCDH001 (Fig. 2) constrain the timing of two magmatic events in the Peake and Denison Domain. A foliated porphyritic granitoid with minor chlorite alteration (Fig. 5a)

records a magmatic age of 1737 ± 6 Ma (Fig. 6a). This magmatism post-dates the *c.* 1780 Ma Wirricurrie Granite and Tidnamurkuna Volcanics recorded in the Denison and Algebuckina inliers (Fig. 2; Ambrose et al., 1981; Rogers and Freeman, 1994; Hopper, 2001; Fanning et al., 2007), but coincides with the age of felsic volcanics from Spring Hills (Fanning et al., 2007) and the likely timing of a tonalite intrusion at Lagoon Hills around *c.* 1730 Ma (Hopper, 2001). This group of igneous ages suggests *c.* 1740 Ma magmatism is dominant in the eastern portion of the Peake and Denison Domain (Fig. 2). The undeformed granitic intrusion records a younger magmatic event at 1466 ± 12 Ma (Fig. 6c). This intrusion crosscuts the foliation in sample R2509358, indicating the foliation formed sometime between *c.* 1740 Ma and *c.* 1470 Ma.

The *c.* 1740 Ma foliated porphyritic granitoid with minor chlorite alteration also yields a younger zircon U–Pb age of 1497 ± 12 Ma (Fig. 6a) from low CL response grains and overgrowths (Fig. 5a). Titanite U–Pb ages obtained from the sample are 1488 ± 13 Ma and 1465 ± 12 Ma (Fig. 6b) from two chemically distinct titanite populations (Fig. 7a). These data were collected from grain mounts, which typically limits age interpretations due to the decoupling of age data from their microstructural context. However, the two generations of titanite in this sample contain distinctly different Fe concentrations, which has a strong influence on the colour and pleochroism of titanite (Deer et al., 2013). In thin section, the titanite grains in this sample have differing pleochroic responses whereby titanite from generation #1 has no pleochroic response and titanite from generation #2 displays some colour change (Fig. 4a). The differences in pleochroic response are interpreted to reflect the contrasting Fe concentrations of the two populations. This allows for microstructural information to be linked to the data collected, which improves the age interpretations for this sample. The first generation of titanite dated at 1487 ± 14 Ma has low Fe concentrations (7500–13,550 ppm; Fig. 7b) and is inferred to come from pale, non-pleochroic grains that commonly form on the edges of magnetite grains in the foliation (Fig. 4a).

The first generation of titanite also has comparatively low U and HREE concentrations (Fig. 7a) that is consistent with a system with limited availability of U and HREEs. These chemical characteristics in titanite are consistent with the coeval growth of a mineral that has a strong affinity for these elements, such as zircon (Rubatto, 2017). This suggests this generation of titanite formed at the same time as the low CL response zircons dated at 1497 ± 12 Ma (Fig. 6a). The second generation of titanite formed at *c.* 1465 Ma has relatively high Fe concentrations (18,200–22,700 ppm; Fig. 7b) and is therefore inferred to be the grains with strong pleochroism that can be observed in the vicinity of chlorite (Fig. 4a). This generation of titanite also has high REE concentrations with similar REE trends to titanite associated with alteration in the other samples in this study (e.g. Fig. 7c, f, g), suggesting they are likely to have formed during alteration.

The hydrothermal titanite U–Pb ages from the altered samples in this study seemingly record a protracted history of hydrothermal activity in the Peake and Denison Domain, with ages that can be grouped into five hydrothermal events at *c.* 1565 Ma, 1530–1515 Ma, *c.* 1500 Ma, *c.* 1465 Ma, and a more recent event at *c.* 490 Ma. However, it is unclear whether the array of early-Mesoproterozoic titanite ages represents a 100-million-year period punctuated by frequent hydrothermal activity, or a series of artificial ages created by partial resetting of the titanite U–Pb isotopic system between events. The youngest Mesoproterozoic alteration ages are recorded in the two drillholes at the northern end of the sampled transect (Fig. 2). Samples R2509358 and R2509354 record alteration ages from titanite at 1465 ± 12 Ma (Fig. 6b) and 1469 ± 11 Ma (Fig. 6e), which coincide with the age of post-deformational magmatism at *c.* 1465 Ma (Fig. 6c) also recorded in this area and therefore are likely related. The titanite alteration ages from drillhole DC09D01 to the south (Fig. 2) show more variation. Sample R2509352 contains textural evidence for two hydrothermal fluid events (Fig. 3g). This sample has an early phase of alteration dominated by clinopyroxene, amphibole, epidote, plagioclase and titanite dated at 1519 ± 8 Ma, that is crosscut by a vein of ilmenite, clinopyroxene, titanite, actinolite and calcite dated at 1494 ± 6 Ma (Figs. 4g and 6h). The age of the vein coincides with the timing of metamorphism recorded by zircon (1497 ± 12 Ma) and titanite (1487 ± 14 Ma) in R2509358 (Fig. 6a, b) and therefore may be associated with that event. The 1519 ± 8 Ma titanite age from the host rock is around the timing of a *c.* 1530 Ma aplitic intrusion at Lagoon Hill (Fanning et al., 2007), and is further validated by clustering of titanite alteration ages at 1532 ± 8 Ma and 1515 ± 7 Ma recorded in the adjacent samples (Fig. 6g, i).

Sample R2509350 provides the oldest titanite alteration age of 1565 ± 6 Ma (Fig. 6f). This age coincides with a granite from Lagoon Hill (Fig. 2) that intruded at 1555 ± 14 Ma (Fanning et al., 2007), which suggests the two may be related. However, it is possible this age could be partially reset given the evidence for alteration of titanite grains in this sample (Fig. 4e) and therefore may represent a minimum age for the oldest alteration event.

A younger hydrothermal fluid event was also identified in drillhole DCDH001, where a brecciated felsic gneiss (Fig. 3c) with a magnetite-biotite-titanite-quartz matrix (Fig. 4c) yields a titanite U–Pb age of *c.* 490 Ma (Fig. 6d). This style of alteration is associated with Cu mineralization in the same drillhole (including a 3-m intercept at 330–333 m grading 2.75% Cu; Ford and Elliston, 1996), suggesting that Cu mineralization occurred during the 515–480 Ma Delamerian Orogeny.

6.2. Evidence for a crustal connection between the NAC and SAC at *c.* 1500 Ma

Palaeoproterozoic connections are already established between the Peake and Denison Domain and Mount Isa Province through the correlation of the *c.* 1780 Ma Tidnamurkuna Volcanics to equivalent volcanic sequences within the Argylla and Bottletree formations in the Mount Isa Province (Wyborn et al., 1987). However, the recognition of *c.* 1740 Ma magmatism in the Peake and Denison Domain and coincident volcanism (Fanning et al., 2007) provides another temporal correlation with the *c.* 1740 Ma Wonga Suite in the Mount Isa Province (Fig. 8; Spence et al., 2022). Magmatism of this age is also recorded in the southeastern Gawler Craton in the McGregor Volcanics and Moonta Porphyry (Fig. 8; Fanning et al., 2007), but it is currently unclear how these systems may be related in a tectonic sense, if at all.

The correlation of events between the NAC and SAC become less clear in the early Mesoproterozoic after around *c.* 1570 Ma following the Kararan/Olarian orogenies in the SAC and the D_1 event of the Isan Orogeny in the Mount Isa Province (Fig. 8). After the Kararan and Olarian orogenies, the evidence for tectonism in the SAC is sporadic until the break-up of Nuna at *c.* 1450 Ma (Fig. 8; Morrissey et al., 2019). However, the lack of evidence for tectonism in the Gawler Craton may be due to the lack of rock exposure in the region. In the southeastern Gawler Craton, magmatism is recorded at *c.* 1560 Ma and *c.* 1515 Ma with the intrusion of the Daly Head Metadolerite and Spilsby Suite, respectively (Jagodzinski et al., 2007; Reid et al., 2022). In the northern Gawler Craton, felsic magmatism is recorded in the Peake and Denison Domain at *c.* 1555 Ma and *c.* 1530 Ma (Fanning et al., 2007), and metamorphism is recorded at *c.* 1500 Ma (Fig. 6a, b). Metamorphism is also recorded in the central northern Gawler Craton at *c.* 1520 Ma (Fig. 8; Reid et al., 2014). In the Mount Isa Province, the 1550–1490 Ma period represents an intense phase of tectonothermal activity involving the voluminous intrusions of the Williams and Naraku batholiths and ongoing orogenesis with the later phases of the Isan Orogeny at *c.* 1550–1490 Ma (Wyborn, 1998; Giles et al., 2006; Rubenach et al., 2008).

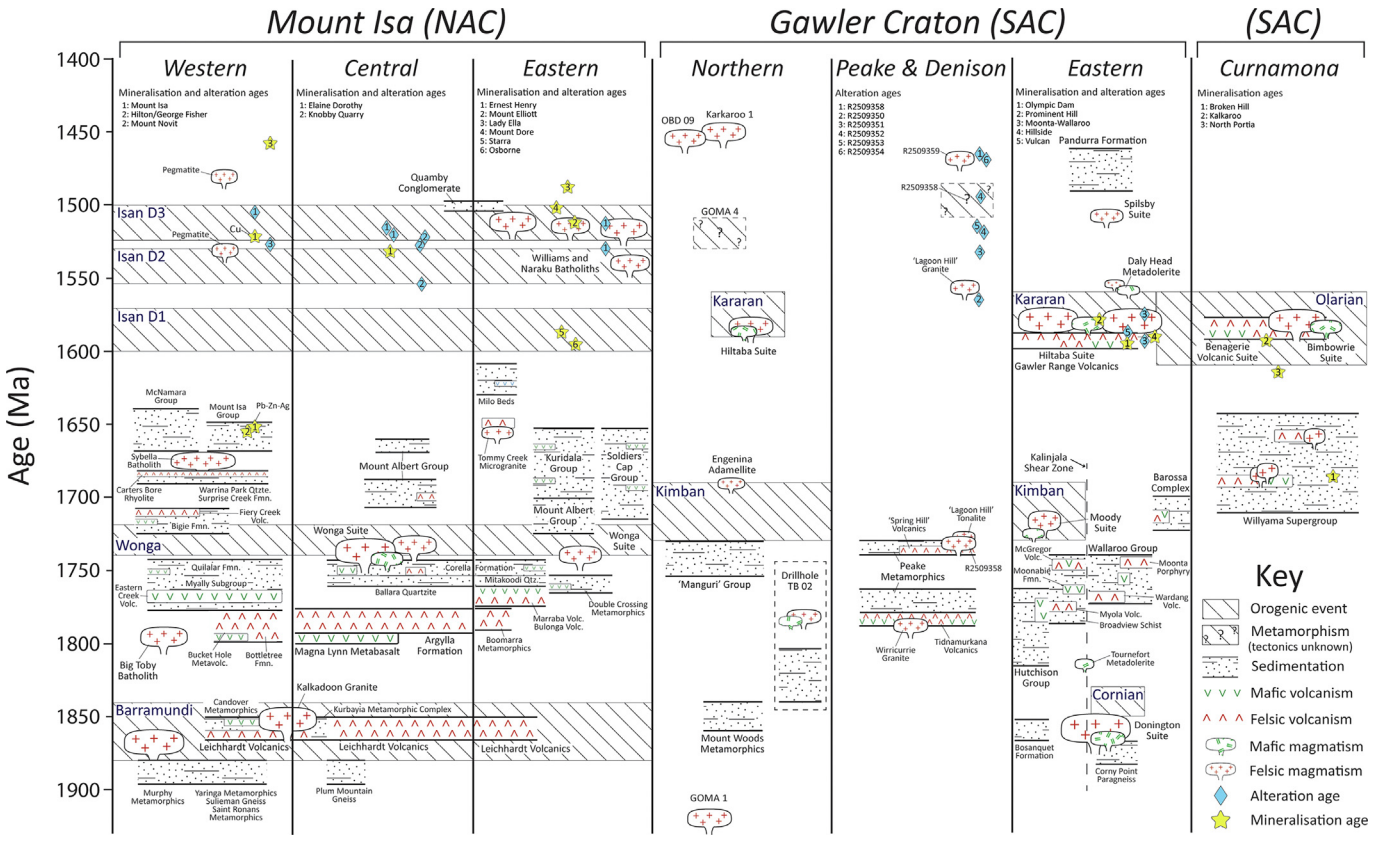

Fig. 8. Simplified time–space plot of the Mount Isa Province (modified from Olierook et al., 2022), Gawler Craton and Curnamona Province (modified from Reid, 2019) with additional data from Connors and Page (1995), Page and Sweet (1998), Perkins et al. (1999), Williams and Skirrow (2000), Gauthier et al. (2001), Page et al. (2005), Mark et al. (2006), Skirrow et al. (2007), Duncan et al. (2011), Gregory et al. (2011), Spandler et al. (2016), Armit et al. (2017), Sawyer et al. (2017), Morrissey et al. (2019).

Hydrothermal alteration in the Mount Isa Province is regionally characterised by early phases of extensive Na-Ca alteration, followed by spatially restricted phases of K ± Fe alteration, sericitisation, silicification, and rare carbonate-muscovite alteration that is intimately associated with Cu-Au mineralization (Duncan et al., 2011; Mark et al., 2006; Oliver et al., 2008; Perkins and Wyborn, 1998; McLellan et al., 2010). An early phase of Na-Ca alteration is recorded in the Eastern Fold Belt at *c.* 1600–1580 Ma and is coeval with mineralization at the Osborne deposit (Fig. 8; Duncan et al., 2011). However, the main phase of alteration and mineralization across the Mount Isa Province is recorded at *c.* 1550–1490 Ma. This is associated with mineralization at Ernest Henry, Mount Elliott, Eloise and Lady Ella deposits in the Eastern Fold Belt (Mark et al., 2006; Duncan et al., 2011), mineralization at Elaine Dorothy in the central Kalkadoon-Leichhardt Domain (Spandler et al., 2016), and epigenetic copper mineralization at the Mount Isa deposit in the Western Fold Belt (Perkins et al., 1999; Mark et al., 2006).

The timing of hydrothermal alteration in the Peake and Denison Domain shows strong correlations with the Mount Isa Province, but not with the Gawler Craton or Curnamona Province (Fig. 8). In addition to this, the calcic nature of alteration in the Peake and Denison Domain has strong resemblance to the characteristic sodic-calcic alteration systems in the Mount Isa Province. The combination of these similarities suggests the Mount Isa Province and Peake and Denison Domain experienced what is effectively the same hydrothermal regime in the early Mesoproterozoic, indicating the NAC and SAC were likely still contiguous within the Diamantina Craton at *c.* 1500 Ma.

6.3. Implications for mineral prospectivity and exploration in the Peake and Denison Domain

The evidence for the connection between the early-Mesoproterozoic hydrothermal systems of the Mount Isa Province and the Peake and Denison Domain suggests the Peake and Denison Domain is prospective for IOCG mineralization akin to that in the Mount Isa Province. Therefore, the knowledge of the controls on IOCG mineralization in the Mount Isa Province can provide a general framework for regional scale mineral exploration in the Peake and Denison Domain.

Copper and gold mineralization in the Mount Isa Province is largely controlled by structures activated during the D_3 stage of the Isan Orogeny at *c.* 1.53–1.50 Ga (Duncan et al., 2011; Mark et al., 2006; Perkins and Wyborn, 1998). During this event the Mount Isa Province experienced E–W directed shortening (Giles et al., 2006), which localised mineralization along broadly N–S (350°–15°) and ENE (40°–75°)-trending structures across the Mount Isa Province (Laing, 1998; Ford and Blenkinsop, 2008; Austin and Blenkinsop, 2009; McLellan et al., 2010). This includes the Mount Isa and Mount Gordon Fault Zones in the Western Fold Belt, and the Selwyn–Mount Dore Corridor in the Eastern Fold Belt, along which many Cu-Au deposits occur (Blake et al., 1990; Duncan et al., 2011). Structural interpretations in the northern Gawler Craton (including the Peake and Denison Domain) are limited due to a lack of exposure. However, the evidence for metamorphism in the northern Gawler Craton at *c.* 1520 Ma (Reid et al., 2014) and the *c.* 1500 Ma foliation in the Peake and Denison Domain (Fig. 6a, b)

indicates there was tectonic activity and associated deformation in the northern Gawler Craton at the time of the D_3 event of the Isan Orogeny (Fig. 8). Therefore, it is possible the Peake and Denison Domain possesses the same structural controls for fluid flow as the Mount Isa Province from the early-Mesoproterozoic. To identify the structures in the Peake and Denison Domain that correspond to the broadly N–S and E–NE trending mineralized structures in the Mount Isa Province, the 51° clockwise rotation of the SAC relative to the NAC since the Mesoproterozoic (Wingate and Evans, 2003; Giles et al., 2004; Payne et al., 2009) must be considered. Due to the locations of the poles used to constrain this rotation in the reconstruction, the structures in the Peake and Denison Domain are offset approximately 30° counterclockwise from their proposed orientations at *c.* 1500 Ma when the Mount Isa Province and Peake and Denison Domain were connected (e.g. Fig. 1b). This would suggest the mineralized N–S (350°–15°) and E–NE (40°–75°)-trending structures in the Mount Isa Province (e.g. McLellan et al., 2010) correspond to the N–NE (20°–45°) and E–W (70°–105°)-trending structures in the Peake and Denison Domain in its present day orientation. Such structures have not been described in the Peake and Denison Domain; however, they may also be difficult to recognise due to overprinting and reactivation during disaggregation of the NAC and SAC at *c.* 1450 Ma (Morrissey et al., 2019), and deformation during the 515–480 Ma Delamerian Orogeny (Foden et al., 2006).

The physical and chemical characteristics of the host lithologies are also considered an important control on IOCG mineralization in the Mount Isa Province. A significant proportion of copper and gold occurrences in the Mount Isa Province exist within 750 m of the contact between the largely calc-silicate rocks of the *c.* 1750–1720 Ma Corella and Staverly formations, and the predominantly siliciclastic *meta*-sedimentary rocks of the *c.* 1680–1650 Ma Soldiers Cap Group (McLellan et al., 2010). The juxtaposition of these lithologies in the presence of strong folding and faulting are suggested to provide a number of key factors that promoted mineralization. These include: (i) favourable sites for fluid mixing and/or fluid–host rock interactions with steep chemical gradients between the *meta*-sedimentary rocks and calc-silicate rocks, (ii) the localisation of fluids at lithological contacts due to strain partitioning caused by significant rheological contrast between the *meta*-sedimentary rocks and calc-silicate rocks, and (iii) a physical barrier for fluid flow between the more permeable *meta*-sedimentary rocks and the less permeable calc-silicate rocks (Oliver et al., 2001; McLellan et al., 2010; Duncan et al., 2014). In addition to their role in providing optimal conditions for mineralization to occur, the metasedimentary rocks in the Mount Isa Province also contain thick scapolite-rich sequences capable of producing highly saline and ligand-rich metamorphic fluids (Morrissey and Tomkins, 2020). These fluids are highly effective in liberating and transporting metals and likely played a role in the formation of the diverse range of mineral deposits in the Mount Isa Province. In the Peake and Denison Domain, interbedded calc-silicate and quartzite sequences in the 1800–1740 Ma Peake Metamorphics contain analogous rock types to the Corella Formation and Soldiers Cap Group in the Mount Isa Province. Such lithologies may have provided the lithological components necessary to replicate the optimal physiochemical crustal conditions for mineralization in the Mount Isa Province.

The intrusion of the 1550–1490 Ma Williams and Naraku batholiths are also considered important for IOCG mineralization in the Mount Isa Province, as a source of fluids and possibly metals (Wyborn, 1998; Bastrakova et al., 2001). In the Peake and Denison Domain, felsic intrusions at *c.* 1555 Ma and *c.* 1530 Ma (Fanning et al., 2007) indicates there are age correlatives to the Williams and Naraku batholiths that may be capable of supplying fluids and possibly metals to mineral systems in the northeastern Gawler Craton. The results of this study indicate there was prolonged hydrothermal activity in the Peake and Denison Domain (Fig. 6e–i) and supports tectonic reconstruction models that place the Peake and Denison Domain at the centre of the Gawler Craton, Mount Isa and Curnamona provinces during the early Mesoproterozoic (Fig. 1b; Giles et al., 2004; Payne et al., 2009; Betts et al., 2015). These factors suggest the prospectivity of the region is unlikely to be limited by lithospheric fertility or metal mobility.

6.4. The utility of tectonic reconstructions for determining mineral prospectivity

The concept of integrating mineral systems into tectonic reconstructions has previously been discussed by Groves and Bierlein (2007). The results of this study not only support this concept, but also demonstrate the utility of this integration for determining mineral prospectivity in greenfields regions for mineral exploration. In this study, the combination of palaeomagnetic constraints and geological correlations provide a robust model for determining terrane-scale prospectivity that is constrained by geometry and geochronology. In the absence of this tectonic reconstruction model linking the northeastern Gawler Craton to the Mount Isa Province (Fig. 1b), it is likely the significance of these results for prospectivity in the Peake and Denison Domain would not be realised, as the *c.* 1550–1500 Ma period is not associated with known mineralization in the Gawler Craton (Fig. 8). This emphasises the utility of tectonic reconstructions for determining prospectivity near the boundaries of crustal blocks, where once cohesive mineral systems may have been fragmented and dispersed by plate tectonics.

7. Conclusion

The correlations between the timing and style of hydrothermal alteration in the Peake and Denison Domain and Mount Isa Province suggests these regions were both influenced by the same hydrothermal systems at *c.* 1565–1500 Ma. This indicates the Gawler Craton and Mount Isa Province were still connected at *c.* 1500 Ma, signifying the NAC and SAC were still contiguous within the Diamantina Craton. The evidence for shared histories between the Peake and Denison Domain and Mount Isa Province from at least *c.* 1780 Ma enhances the mineral potential of the Peake and Denison Domain, as it is more likely to have inherited many of the crustal characteristics that provided important lithological controls on IOCG mineralization in the Mount Isa Province. Furthermore, evidence for hydrothermal events around *c.* 1460 and *c.* 490 Ma in the Peake and Denison Domain emphasises additional opportunities for mineralization events in the northeastern Gawler Craton. Further work on understanding the structural relationships between the Peake and Denison Domain and Mount Isa Province to improve the reconstruction of their early-Mesoproterozoic configuration would add considerable value to IOCG mineral exploration in the northeastern Gawler Craton.

CRediT authorship contribution statement

Mitchell J. Bockmann: Investigation, Writing – original draft, Formal analysis, Visualization. **Justin L. Payne:** Conceptualization, Investigation, Writing – review & editing, Supervision, Funding acquisition. **Martin Hand:** Conceptualization, Writing – review & editing, Supervision, Funding acquisition. **Laura J. Morrissey:** Conceptualization, Writing – review & editing, Supervision. **Antonio P. Belperio:** Resources, Writing – review & editing.

Declaration of Competing Interest

The authors declare that they have no known competing financial interests or personal relationships that could have appeared to influence the work reported in this paper.

Acknowledgements

S. Gilbert from Adelaide Microscopy is gratefully acknowledged for her assistance in the development of titanite U–Pb geochronology protocols and data collection using LA-ICP-MS at Adelaide Microscopy. C. Spandler is thanked for providing helpful comments on an early version of this manuscript and R. Flint (then of Minotaur Exploration) is thanked for his assistance in sampling. C. Tiddy and an anonymous reviewer are thanked for their constructive review comments and V.O. Samuel is thanked for editorial handling. This work has been supported by ARC Linkage Project LP160100578 (JLP and MH) and the Mineral Exploration Cooperative Research Centre whose activities are funded by the Australian Government's Cooperative Research Centre Program. MJB acknowledges the support of an Australian Government Research Training Program Stipend and LJM acknowledges the support of ARC DECRA Fellowship DE210101126. This is MinEx CRC Document 2022/79.

Appendix A. Supplementary data

Supplementary data to this article can be found online at https://doi.org/10.1016/j.gsf.2023.101596.

References

Ambrose, G.J., Flint, R.B., Webb, A.W., 1981. Precambrian and Palaeozoic geology of the Peake and Denison ranges, Adelaide, Australia. In: Geological Survey of South Australia. Bulletin, p. 50.

Armit, R., Betts, P., Schaefer, B., Yi, K., Kim, Y., Dutch, R.A., Reid, A., Jagodzinski, L., Giles, D., Ailleres, L., 2017. Late Palaeoproterozoic evolution of the buried northern Gawler Craton. Precambr. Res. 291, 178–201.

Austin, J.R., Blenkinsop, T.G., 2009. Local to regional scale structural controls on mineralisation and the importance of a major lineament in the eastern Mount Isa Inlier, Australia: Review and analysis with autocorrelation and weights of evidence. Ore Geol. Rev. 35 (3), 298–316.

Betts, P., Armit, R., Stewart, J., Aitken, A., Ailleres, L., Donchak, P., Hutton, L., Withnall, I., Giles, D., 2015. Australia and nuna. Geol. Soc. London, Spec. Pub. 424, p. SP424. 422.

Betts, P., Giles, D., 2006. The 1800–1100Ma tectonic evolution of Australia. Precambr. Res. 144 (1), 92–125.

Bastrakova, I.V., Budd, A.R., Wyborn, L.A.I., 2001. The metallogenic potential of Australian Proterozoic granites GIS data package. Geoscience Australia, Canberra. http://pid.geoscience.gov.au/dataset/ga/36204.

Betts, P., Aillères, L., Hulscher, B., Hough, M., Lister, G.S., 2006. Evolution of the Isan Orogeny at the southeastern margin of the Mt Isa Inlier AU - Giles, D. Aust. J. Earth Sci. 53 (1), 91–108.

Beyer, S., Kyser, K., Polito, P., Fraser, G., 2018. Mesoproterozoic rift sedimentation, fluid events and uranium prospectivity in the Cariewerloo Basin, Gawler Craton, South Australia. Austral. J. Earth Sci. 65 (3), 409–426.

Bierlein, F.P., Black, L.P., Hergt, J., Mark, G., 2008. Evolution of Pre-1.8 Ga basement rocks in the western Mt Isa Inlier, northeastern Australia—insights from SHRIMP U-Pb dating and in-situ Lu–Hf analysis of zircons. Precambr. Res. 163 (1–2), 159–173.

Blake, D., Etheridge, M., Page, R., Stewart, A., Williams, P., Wyborn, L., 1990. Mount Isa Inlier—regional geology and mineralisation. In: Geology of the mineral deposits of Australia and Papua New Guinea, pp. 915–923.

Cawood, P.A., Hawkesworth, C.J., 2015. Temporal relations between mineral deposits and global tectonic cycles. Geol. Soc. London, Spec. Publ. 393 (1), 9–21.

Cawood, P.A., Korsch, R., 2008. Assembling Australia: Proterozoic building of a continent. Precambr. Res. 166 (1–4), 1–35.

Connors, K.A., Page, R.W., 1995. Relationships between magmatism, metamorphism and deformation in the western Mount Isa Inlier, Australia. Precambrian Res. 71, 131–153.

Conor, C.H.H., Preiss, W.V., 2008. Understanding the 1720–1640 Ma Palaeoproterozoic Willyama Supergroup, Curnamona Province, southeastern Australia: Implications for tectonics, basin evolution and ore genesis. Precambr. Res. 166, 297–317.

Daly, S., 1998. Tectonic evolution and exploration potential of the Gawler Craton, South Australia: AGSO. AGSO J. Aust. Geol. Geophys. 17, 145–168.

Deer, W., Howie, R., Zussman, J., 2013. An introduction to the rock-forming minerals. The Mineralogical Society, London, UK, 498 pp.

Duncan, R.J., Stein, H.J., Evans, K.A., Hitzman, M.W., Nelson, E.P., Kirwin, D.J., 2011. A new geochronological framework for mineralization and alteration in the Selwyn-Mount Dore corridor, Eastern fold belt, Mount Isa inlier, Australia: Genetic implications for iron oxide copper-gold deposits. Econ. Geol. 106 (2), 169–192.

Duncan, R.J., Hitzman, M.W., Nelson, E.P., Togtokhbayar, O., 2014. Structural and Lithological Controls on Iron Oxide Copper-Gold Deposits of the Southern Selwyn-Mount Dore Corridor, Eastern Fold Belt, Queensland, Australia. Econ. Geol. 109 (2), 419–456.

Dutch, R., Hand, M., Kinny, P.D., 2008. High-grade Paleoproterozoic reworking in the southeastern Gawler Craton, South Australia. Austral. J. Earth Sci. 55, 1063–1081.

Elburg, M., Bons, P., Foden, J., Brugger, J., 2003. A newly defined Late Ordovician magmatic-thermal event in the Mt Painter Province, northern Flinders Ranges, South Australia. Austral. J. Earth Sci. 50 (4), 611–631.

Fanning, C.M., Flint, R.B., Parker, A.J., Ludwig, K.R., Blissett, A.H., 1988. Refined Proterozoic evolution of the Gawler Craton, South Australia, through U-Pb zircon geochronology. Precambr. Res. 40–41, 363–386.

Fanning, C.M., Reid, A., Teale, G.S., 2007. A geochronological framework for the Gawler Craton. Geological Survey, South Australia, South Australia, p. 258.

Foden, J., Elburg, M.A., Dougherty-Page, J., Burtt, A., 2006. The timing and duration of the Delamerian Orogeny: correlation with the Ross Orogen and implications for Gondwana assembly. J. Geol. 114 (2), 189–210.

Ford, J., and Elliston, A., 1996, Annual Report for Kingston North and Davenport Creek Prospects, Peake and Denison Ranges: EL 1844 and EL 1925.

Ford, A., Blenkinsop, T.G., 2008. Combining fractal analysis of mineral deposit clustering with weights of evidence to evaluate patterns of mineralization: Application to copper deposits of the Mount Isa Inlier, NW Queensland, Australia. Ore Geol. Rev. 33 (3), 435–450.

Foster, D.R., Austin, J.R., 2008. The 1800–1610 Ma stratigraphic and magmatic history of the Eastern Succession, Mount Isa Inlier, and correlations with adjacent Paleoproterozoic terranes. Precambr. Res. 163 (1–2), 7–30.

Fraser, G., Lyons, P., 2006. Timing of Mesoproterozoic tectonic activity in the northwestern Gawler Craton constrained by $^{40}Ar/^{39}Ar$ geochronology. Precambr. Res. 151, 160–184.

Fraser, G.L., Reid, A.J., Stern, R.J., 2012. Timing of deformation and exhumation across the Karari Shear Zone, north-western Gawler Craton, South Australia. Austral. J. Earth Sci. 59, 547–570.

Gauthier, L., Hall, G., Stein, H., Schaltegger, Urs., 2001. The Osborne Deposit, Cloncurry District; a 1595 Ma Cu–Au skarn deposit. Contributions of the Economic Geology Research Unit 59, 58–59.

Gehrels, G.E., Valencia, V.A., Ruiz, J., 2008. Enhanced precision, accuracy, efficiency, and spatial resolution of U-Pb ages by laser ablation–multicollector–inductively coupled plasma–mass spectrometry. Geochem. Geophys. Geosyst. (3), Q03017. https://doi.org/10.1029/2007GC001805.

Giles, D., Betts, P.G., Lister, G.S., 2004. 1.8–1.5-Ga links between the North and South Australian Cratons and the Early-Middle Proterozoic configuration of Australia. Tectonophysics 380 (1), 27–41.

Giles, D., Betts, P.G., Aillères, L., Hulscher, B., Hough, M., Lister, G., 2006. Evolution of the Isan Orogeny at the southeastern margin of the Mt Isa Inlier. Aust. J. Earth Sci. 53 (1), 91–108.

Groves, D.I., Bierlein, F.P., 2007. Geodynamic settings of mineral deposit systems. J. Geol. Soc. London 164 (1), 19–30.

Hand, M., Reid, A., Jagodzinski, E., 2007. Tectonic framework and evolution of the Gawler Craton, South Australia. Econ. Geol. 102, 1377–1395.

Hollis, J., Beyer, E., Whelan, J., Kemp, A., Scherstén, A., and Greig, A., 2010, Summary of results. NTGS laser U-Pb and Hf geochronology project: Pine Creek Orogen, Murphy Inlier, McArthur Basin and Arunta Region, July 2007–June 2008: Northern Territory Geological Survey, Record, v. 1.

Hopper, D.J., 2001. Crustal evolution of Palaeo- to Mesoproterozoic rocks in the Peake and Denison Ranges. Ph.D thesis, University of Queensland, South Australia, 216 pp.

Howard, K.E., Hand, M., Barovich, K.M., Payne, J.L., Belousova, E.A., 2011a. U-Pb, Lu–Hf and Sm–Nd isotopic constraints on provenance and depositional timing of metasedimentary rocks in the western Gawler Craton: implications for Proterozoic reconstruction models. Precambr. Res. 184 (1–4), 43–62.

Howard, K.E., Hand, M., Barovich, K.M., Payne, J.L., Cutts, K.A., Belousova, E.A., 2011b. U-Pb zircon, zircon Hf and whole-rock Sm–Nd isotopic constraints on the evolution of Paleoproterozoic rocks in the northern Gawler Craton. Aust. J. Earth Sci. 58 (6), 615–638.

Howard, H., Smithies, R., Kirkland, C., Kelsey, D., Aitken, A., Wingate, M., De Gromard, R.Q., Spaggiari, C., Maier, W.D., 2015. The burning heart—the Proterozoic geology and geological evolution of the west Musgrave Region, central Australia. Gondw. Res. 27 (1), 64–94.

Jackson, S.E., Pearson, N.J., Griffin, W.L., Belousova, E.A., 2004. The application of laser ablation-inductively coupled plasma-mass spectrometry to in situ U-Pb zircon geochronology. Chem. Geol. 211 (1–2), 47–69.

Jackson, M., Sweet, I., Page, R., Bradshaw, B., 1999. The South Nicholson and Roper Groups: evidence for the early Mesoproterozoic Roper Superbasin: Integrated Basin Analysis of the Isa Superbasin using Seismic, Well-log, and Geopotential Data: An Evaluation of the Economic Potential of the Northern Lawn Hill Platform: Canberra. Australian Geological Survey Organisation Record, Australia.

Jackson, M., Scott, D., Rawlings, D., 2000. Stratigraphic framework for the Leichhardt and Calvert Superbasins: Review and correlations of the pre-1700 Ma successions between Mt Isa and McArthur River. Aust. J. Earth Sci. 47 (3), 381–403.

Jagodzinski, E. A., Reid, A. J., Chalmers, N. C., Swain, G., Frew, R. A., and Foudoulis, C., 2007, Compilation of SHRIMP U-Pb geochronological data for the Gawler Craton, South Australia, 2007: South Australia. Department of Primary Industries and Resources. Report Book 2007/21.

Jochum, K.P., Weis, U., Stoll, B., Kuzmin, D., Yang, Q., Raczek, I., Jacob, D.E., Stracke, A., Birbaum, K., Frick, D.A., 2011. Determination of reference values for NIST SRM 610–617 glasses following ISO guidelines. Geostand. Geoanal. Res. 35 (4), 397–429.

Laing, W., 1998. Structural-metasomatic environment of the East Mt Isa Block base-metal-gold province. Aust. J. Earth Sci. 45 (3), 413–428.

Mark, G., Oliver, N.H., Williams, P.J., 2006. Mineralogical and chemical evolution of the Ernest Henry Fe oxide–Cu–Au ore system, Cloncurry district, northwest Queensland, Australia. Mineral. Deposita 40 (8), 769.

McDonald, G.D., Collerson, K.D., Kinny, P.D., 1997. Late Archean and early Proterozoic crustal evolution of the Mount Isa block, northwest Queensland, Australia. Geology 25 (12), 1095–1098.

McLellan, J. G., Mustard, R., Blenkinsop, T., Oliver, N. H., and McKeagney, C., 2010. Critical ingredients of IOCG mineralisation in the Eastern Fold Belt of the Mount Isa Inlier: insights from combining spatial analysis with mechanical numerical modelling. PGC Publishing.

Morrissey, L.J., Barovich, K.M., Hand, M., Howard, K.E., Payne, J.L., 2019. Magmatism and metamorphism at ca. 1.45 Ga in the northern Gawler Craton: The Australian record of rifting within Nuna (Columbia). Geosci. Front. 10 (1), 175–194.

Morrissey, L.J., Tomkins, A.G., 2020. Evaporite-bearing orogenic belts produce ligand-rich and diverse metamorphic fluids. Geochim. Cosmochim. Acta 275, 163–187.

Neumann, N.L., Gibson, G.M., Southgate, P.N., 2009. New SHRIMP age constraints on the timing and duration of magmatism and sedimentation in the Mary Kathleen Fold Belt, Mt Isa Inlier, Australia. Austral. J. Earth Sci. 56 (7), 965–983.

Neumann, N., Southgate, P., Gibson, G., McIntyre, A., 2006. New SHRIMP geochronology for the Western Fold Belt of the Mt Isa Inlier: developing a 1800–1650 Ma event framework. Aust. J. Earth Sci. 53 (6), 1023–1039.

Norris, A., Danyushevsky, L., 2018. Towards Estimating the Complete Uncertainty Budget of Quantified Results Measured by LA-ICPMS. Goldschmidt, Boston, MA, USA.

Olierook, H.K., Mervine, E.M., Armstrong, R., Duckworth, R., Evans, N.J., McDonald, B., Kirkland, C.L., Kumara, A.S., Wood, D.G., Cristall, J., 2022. Uncovering the Leichhardt Superbasin and Kalkadoon-Leichhardt Complex in the southern Mount Isa Terrane, Australia. Precambr. Res. 375, 106680.

Oliver, N.H., Butera, K.M., Rubenach, M.J., Marshall, L.J., Cleverley, J.S., Mark, G., Tullemans, F., Esser, D., 2008. The protracted hydrothermal evolution of the Mount Isa Eastern Succession: A review and tectonic implications. Precambr. Res. 163 (1–2), 108–130.

Oliver, N.H.S., Ord, A., Valenta, R.K., Upton, P., Richards, J.P., Tosdal, 2001. Deformation, Fluid Flow, and Ore Genesis in Heterogeneous Rocks, with Examples and Numerical Models from the Mount Isa District, Australia. In: Richards, J.P, Tosdal, R.M. (Eds.), Structural Controls on Ore Genesis. Society of Economic Geologists. https://doi.org/10.5382/Rev.14.03.

Page, R.W., Stevens, B.P.J., Gibson, G.M., 2005. Geochronology of the Sequence Hosting the Broken Hill Pb-Zn-Ag Orebody, Australia. Econ. Geol. 100 (4), 633–661.

Page, R.W., Sweet, I.P., 1998. Geochronology of basin phases in the western Mt Isa Inlier, and correlation with the McArthur Basin. Aust. J. Earth Sci. 45 (2), 219–232.

Paton, C., Hellstrom, J., Paul, B., Woodhead, J., Hergt, J., 2011. Iolite: Freeware for the visualisation and processing of mass spectrometric data. J. Anal. At. Spectrom 26 (12), 2508–2518.

Payne, J.L., Barovich, K.M., Hand, M., 2006. Provenance of metasedimentary rocks in the northern Gawler Craton, Australia: Implications for Palaeoproterozoic reconstructions. Precambr. Res. 148 (3), 275–291.

Payne, J.L., Hand, M., Barovich, K.M., Reid, A., Evans, D.A., 2009. Correlations and reconstruction models for the 2500–1500 Ma evolution of the Mawson Continent. Geol. Soc. London, Spec. Pub. 323 (1), 319–355.

Perkins, C., Heinrich, C.A., Wyborn, L.A., 1999. 40 Ar/39 Ar geochronology of copper mineralization and regional alteration, Mount Isa, Australia. Econ. Geol. 94 (1), 23–36.

Perkins, C., Wyborn, 1998. Age of Cu-Au mineralisation, Cloncurry district, eastern Mt Isa Inlier, Queensland, as determined by 40Ar/39Ar dating. Australian Journal of Earth Sciences 45 (2), 233–246. https://doi.org/10.1080/08120099808728384.

Reid, A., 2019. The Olympic Cu-Au Province, Gawler Craton: a review of the lithospheric architecture, geodynamic setting, alteration systems, cover successions and prospectivity. Minerals 9, 371.

Reid, A.J., Jagodzinski, E.A., Wade, C.E., Payne, J.L., Jourdan, F., 2017. Recognition of c. 1780 Ma magmatism and metamorphism in the buried northeastern Gawler Craton: correlations with events of the Aileron Province. Precambrian Res. 302, 198–220.

Reid, A., Hand, M., Jagodzinski, E., Kelsey, D., Pearson, N.J., 2008. Palaeoproterozoic orogenesis within the southeastern Gawler Craton, South Australia. Austral. J. Earth Sci. 55, 449–471.

Reid, A., Hand, M., 2012. Mesoarchaean to Mesoproterozoic evolution of the southern Gawler Craton, South Australia. Episodes 35 (1), 216–225.

Reid, A.J., Jagodzinski, E.A., Armit, R.J., Dutch, R.A., Kirkland, C.L., Betts, P.G., Schaefer, B.F., 2014. U-Pb and Hf isotopic evidence for Neoarchaean and Palaeoproterozoic basement in the buried northern Gawler Craton, South Australia. Precambr. Res. 250, 127–142.

Reid, A.J., Wade, C.E., Jagodzinski, E.A., 2022. Mafic dykes of the southeastern Gawler Craton: *ca* 1564 Ma magmatism with an enriched mantle source. Aust. J. Earth 69 (5), 711–732.

Rogers, P., and Freeman, P., 1994, Explanatory notes for the Warrina 1:250 000 Geological Map. South Australian Department of Mines and Energy, Report Book 93/10.

Rubatto, D., 2017. Zircon: The metamorphic mineral. Rev. Mineral. Geochem. 83, 261–295.

Rubenach, M.J., Foster, D., Evins, P., Blake, K., Fanning, C., 2008. Age constraints on the tectonothermal evolution of the Selwyn Zone, Eastern fold belt, Mount Isa Inlier. Precambr. Res. 163 (1–2), 81–107.

Sawyer, M., Whittaker, B., and de Little, J., 2017, Carrapateena iron oxide Cu-Au-Ag-U deposit: in Phillips, G.N., (Ed.), 2017 Australian Ore Deposits, The Australiasian Institute of Mining and Metallurgy, Mono 32, p. 615-620.

Skirrow, R., Ashley, P., McNaughton, N., Suzuki, K., 2000. Time–space framework of Cu–Au–(Mo) and regional alteration systems in the Curnamona Province. Austral. Geol. Survey Org. Rec. 10, 83–86.

Skirrow, R.G., Bastrakov, E., Barovich, K., Fraser, G., Fanning, C.M., Creaser, R., Davidson, G., 2007. Timing of Iron Oxide Cu-Au-(U) Hydrothermal Activity and Nd Isotope Constraints on Metal Sources in the Gawler Craton, South Australia. Econ. Geol. 102, 1441–1470.

Skirrow, R., van der Wielen, S.E., Champion, D.C., Czarnota, K., Thiel, S., 2018. Lithospheric artchitecture and mantle metasomatism linked to iron-oxide Cu-Au ore formation: Multidiciplinary evidence from the Olympic Dam region, South Australia. Geochem. Geophys. Geosyst., 19

Sláma, J., Košler, J., Condon, D.J., Crowley, J.L., Gerdes, A., Hanchar, J.M., Horstwood, M.S., Morris, G.A., Nasdala, L., Norberg, N., 2008. Plešovice zircon—a new natural reference material for U-Pb and Hf isotopic microanalysis. Chem. Geol. 249 (1–2), 1–35.

Spandler, C., Hammerli, J., Sha, P., Hilbert-Wolf, H., Hu, Y., Roberts, E., Schmitz, M., 2016. MKED1: a new titanite standard for in situ analysis of Sm–Nd isotopes and U-Pb geochronology. Chem. Geol. 425, 110–126.

Spence, J.S., Sanislav, I.V., Dirks, 2022. Evidence for a 1750–1710 Ma orogenic event, the Wonga Orogeny, in the Mount Isa Inlier, Australia: Implications for the tectonic evolution of the North Australian Craton and Nuna Supercontinent. Precambrian Research 369, 106510.

Stevens, B., Page, R., Crooks, A., 2008. Geochronology of Willyama Supergroup metavolcanics, metasediments and contemporaneous intrusions, Broken Hill, Australia. Austral. J. Earth Sci. 55 (3), 301–330.

Swain, G., Hand, M., Teasdale, J., Rutherford, L., Clark, C., 2005. Age constraints on terrane-scale shear zones in the Gawler Craton, southern Australia. Precamb. Res. 139, 164–180.

Szpunar, M., Hand, M., Barovich, K., Jagodzinski, E., Belousova, E., 2011. Isotopic and geochemical constraints on the Paleoproterozoic Hutchison Group, southern Australia: Implications for Paleoproterozoic continental reconstructions. Precambr. Res. 187 (1–2), 99–126.

Tucker, N.M., Hand, M., Kelsey, D.E., Dutch, R.A., 2015. A duality of timescales: Short-lived ultrahigh temperature metamorphism preserving a long-lived monazite growth history in the Grenvillian Musgrave–Albany–Fraser Orogen. Precambr. Res. 264, 204–234.

Vermeesch, P., 2018. IsoplotR: A free and open toolbox for geochronology. Geosci. Front. 9 (5), 1479–1493.

Wade, C.E., Reid, A., Wingate, M.T.D., Jagodzinski, E.A., Barovich, K., 2012. Geochemistry and geochronology of the c. 1585 Ma Benagerie Volcanic Suite, southern Australia: relationship to the Gawler Range Volcanics and implications for the petrogenesis of a Mesoproterozoic silicic large igneous province. Precamb. Res. 206–207, 17–35.

Wiedenbeck, M., Alle, P., Corfu, F., Griffin, W., Meier, M., Oberli, F.V., Quadt, A.V., Roddick, J., Spiegel, W., 1995. Three natural zircon standards for U-Th-Pb, Lu-Hf, trace element and REE analyses. Geostandards Newslett. 19 (1), 1–23.

Williams, P.J., Skirrow, R.G., 2000. Overview of iron oxide-copper–gold deposits in the Curnamona Province and Cloncurry district (Eastern Mount Isa Block), Australia. In: Porter, T.M. (Ed.), Hydrothermal Iron Oxide Copper–Gold and Related Deposits: A Global Perspective V1. PGC Publishing, Adelaide, pp. 105–122.

Wingate, M.T., Evans, D.A., 2003. Palaeomagnetic constraints on the Proterozoic tectonic evolution of Australia. Geol. Soc. London, Spec. Publ. 206 (1), 77–91.

Wyborn, L., 1998. Younger ca 1500 Ma granites of the Williams and Naraku Batholiths, Cloncurry district, eastern Mt Isa Inlier: geochemistry, origin, metallogenic significance and exploration indicators. Aust. J. Earth Sci. 45 (3), 397–411.

Wyborn, L.A.I., Heinrich, C.A. and Jaques, A.L., 1994. Australian Proterozoic Mineral Systems: Essential Ingredients and Mappable Criteria. In: Proceedings of the Australian Institute of Miningand Metallurgy Annual Conference, Melbourne, pp. 109-115.

Wyborn, L.A.I., Page, R.W., Parker, A.J., 1987. Geochemical and geochronological signatures in Australian Proterozoic igneous rocks. Geol. Soc. London, Spec. Pub. 33, 377–394.